Detection possibility of a pseudo-FIMP in the presence of a thermal WIMP

Subhaditya Bhattacharya,[1,*] Jayita Lahiri,[2,†] and Dipankar Pradhan[1,‡]
[1]Department of Physics, Indian Institute of Technology Guwahati, Assam-781039, India
[2]Institut für Theoretische Physik, Universität Hamburg, 22761 Hamburg, Germany

(Received 19 January 2024; accepted 26 April 2024; published 21 May 2024)

A dark matter (DM) having feeble interaction with the visible sector can thermalize via substantial interaction with a weakly interacting massive particle (WIMP). Such DM candidates can be categorized as pseudofeebly interacting massive particles (pFIMPs). pFIMPs have both direct and indirect search prospects via a WIMP loop. This work focuses on such possibilities. We provide all such one loop graphs stemming from pFIMP-WIMP interactions involving scalar, fermion, and vector boson particles, assuming both of them are stabilized via $\mathbb{Z}_2 \otimes \mathbb{Z}_2'$ symmetries. We elaborate upon a model where a fermionic WIMP has a significant Yukawa interaction with a scalar pFIMP with negligible Higgs portal coupling. We study, in detail, the loop induced direct and indirect search prospects of the pFIMP in the relic density allowed region of the model along with collider expectations at the LHC.

DOI: 10.1103/PhysRevD.109.095031

I. INTRODUCTION

Particle dark matter (DM) has long been studied as it caters to most of the astrophysical and cosmological observations in a consistent manner. Apart from the electromagnetic charge neutrality and stability over the scale of the Universe's lifetime, there are not many unique characteristics that can be assigned to a DM particle. There emerges many possibilities for how it saturates the observed relic density, given by the Planck data ($\Omega_{\rm DM}h^2 = 0.1200 \pm 0.0012$ [1]). In one class of models, the DM remains in equilibrium with the thermal bath due to sizeable interaction with the visible sector. Then it freezes out as the Universe expands and cools down. If the depletion occurs via $2_{\rm DM} \to 2_{\rm SM}$ process, then the annihilation cross section required for the DM to attain correct relic density is of the order of electroweak interaction ($\sim 10^{-10}$ GeV^{-2}). Hence, such particles are dubbed as weakly interacting massive particles (WIMPs) [2,3]. In some cases the number changing processes are governed mainly within the dark sector via $3_{\rm DM} \to 2_{\rm DM}$ or $4_{\rm DM} \to 2_{\rm DM}$ processes; the annihilation cross section is then required to be much larger to adjust the additional phase space suppression and such a class of DM particles are called strongly interacting massive particles (SIMPs) [4]. The other possibility is to assume the DM having a feeble interaction with the visible sector, so that it remains out of equilibrium and gets produced via decay or annihilation of thermal bath particles and saturates when the temperature drops below the DM mass. Such particles are called feebly interacting massive particles (FIMPs) [5]. Several other possibilities like self-interacting DM [6,7], cannibal DM [8], etc. have also been ideated. Our discussion here will be centered around WIMPs and FIMPs that arise in extension of the Standard Model (SM).

DM detectability is also quite different for these class of particles. WIMPs having sizeable interaction with the SM and can provide a nuclear/electron recoil signal in direct DM search experiments like XENON [9–12], PandaX [13,14], LUX-ZEPLIN [15], etc., although not found yet. Similar signals for a FIMP or a SIMP are often difficult due to the small interaction with the SM. Collider search for DM has been studied extensively, where the DM after being produced, carries away missing momentum or energy in the presence of visible leptons, photons, or jets, both at the LHC [16–24] and international linear collider [25–31]. Again, WIMPs have the best bet to provide such signals [3,32], while the disappearing charge track or displaced vertex signal can sometimes indicate the presence of FIMPs, see for example, [33]. However, null observation in both direct and collider searches put bounds on the available DM parameter space. Apart from these terrestrial DM search experiments, indirect search for DM stemming from its annihilation into photon [34,35], antiproton [36–39], or positron [40–42] via their excess fluxes in the center of galaxies have been studied. Again, FIMP/SIMP types of DMs are difficult to probe via indirect search as well.

*subhab@iitg.ac.in
†jayita.lahiri@desy.de
‡d.pradhan@iitg.ac.in

A dark sector consisting of more than one DM component is the focus of the current paper. Two-component DM models are proposed in various contexts [43–46] and have been extensively studied [47–49]. They provide many new features, a crucial one being the issue of DM-DM interaction or conversion. WIMP-WIMP models show features like modified freeze-out, modified direct search prospects [46], and double bump distribution in the missing energy signal at the collider [50,51]. A recent study shows that the interaction between two FIMPs can cater to structure formation issues [52]. In WIMP-FIMP models, the conversion process helps in FIMP production from the WIMP, but does not affect the WIMP phenomenology when the interaction is feeble. When the interaction is of the weak interaction strength, it brings the FIMP to thermal bath, as shown in [53]; it is then called pseudo-FIMP or pFIMP. pFIMPs always rely on the conversion process for their freeze-out, and this makes them distinct from the WIMPs. Some pFIMP scenarios have been studied in [46–48], without detailing on the potential characteristics or phenomenological consequences.

We study here a two component DM model with one scalar and one fermion. The scalar sector consists of a singlet and is assumed to be the pFIMP component. The fermion sector consists of a vectorlike doublet and a singlet, where the lightest state after mixing via electroweak symmetry breaking (EWSB) serves as the WIMP component having gauge interaction with the visible sector.[1] The possibility of bringing the fermion pFIMP under the direct search scanner via WIMP loop has been studied here in detail with some discussions on the indirect search prospects.

The paper is organized as follows. In Sec. II, we present a general discussion on the WIMP-pFIMP scenario and possible interactions between the WIMP and pFIMP that can give rise to the pFIMP detection prospect. In Sec. III, we discuss a model example in WIMP-pFIMP limit. The DM phenomenology, including relic density, direct (indirect), and collider detection prospects, are discussed in Sec. IV. In Sec. V, we summarize and conclude. Several appendices provide the details of the relevant calculations.

II. WIMP-PFIMP ENSEMBLE

A DM having feeble interaction with the SM can still thermalize via sizeable interaction with a WIMP and is called a pFIMP as demonstrated in [53]. We first provide a short account of this set up and the resulting behavior of the pFIMP.

A. Generic pFIMP characteristics

Most of the pFIMP characteristics can be described in a model independent way where the freeze-out pattern of both the WIMP and pFIMP are governed via a generic coupled Boltzmann equation (cBEQ),

$$\frac{d\mathrm{Y}_1}{dx} = -\frac{2\pi^2 \mathrm{M_{pl}}}{45\times 1.66}\frac{g^s_\star}{\sqrt{g^\rho_\star}}\frac{\mu_{12}}{x^2}\left[\langle\sigma v\rangle_{11\to \mathrm{SM}}(\mathrm{Y}_1^2 - Y_1^{\mathrm{eq}^2}) + \langle\sigma v\rangle_{11\to 22}\left(\mathrm{Y}_1^2 - \frac{Y_1^{\mathrm{eq}^2}}{Y_2^{\mathrm{eq}^2}}\mathrm{Y}_2^2\right)\right],$$
$$\frac{d\mathrm{Y}_2}{dx} = \frac{2\mathrm{M_{pl}}}{1.66\times\sqrt{g^\rho_\star}}\frac{x}{\mu_{12}^2}\langle\Gamma_{\mathrm{SM}\to 22}\rangle\left(Y^{\mathrm{eq}}_{\mathrm{SM}} - \frac{\mathrm{Y}_2^2}{Y_2^{\mathrm{eq}^2}}Y^{\mathrm{eq}}_{\mathrm{SM}}\right) + \frac{4\pi^2\mathrm{M_{pl}}}{45\times 1.66}\frac{g^s_\star}{\sqrt{g^\rho_\star}}\frac{\mu_{12}}{x^2}\left[\langle\sigma v\rangle_{\mathrm{SM}\to 22}\left(Y^{\mathrm{eq}^2}_{\mathrm{SM}} - \frac{\mathrm{Y}_2^2}{Y_2^{\mathrm{eq}^2}}Y^{\mathrm{eq}^2}_{\mathrm{SM}}\right)\right.$$
$$\left. + \langle\sigma v\rangle_{11\to 22}\left(\mathrm{Y}_1^2 - \frac{Y_1^{\mathrm{eq}^2}}{Y_2^{\mathrm{eq}^2}}\mathrm{Y}_2^2\right)\right]. \tag{1}$$

In the above and also in the rest of the draft, $\mathrm{M_{pl}} = 1.22091\times 10^{19}$ GeV represents Planck mass, $g^s_\star \simeq g^\rho_\star \approx 106.7$ denotes effective massless degrees of freedom, and subscripts 1(2) denote WIMP(pFIMP). The interaction channels which govern the freeze-out/freeze-in of the DM components are:

(i) $\langle\sigma v\rangle_{11\to \mathrm{SM}}$: annihilation/depletion of the WIMP to the SM states.
(ii) $\langle\sigma v\rangle_{11\to 22}$: conversion of the WIMP to the FIMP (pFIMP) or vice versa.
(iii) $\langle\sigma v\rangle_{\mathrm{SM}\to 22}$: production of the FIMP (pFIMP) from the thermal (SM) bath.
(iv) $\langle\Gamma_{\mathrm{SM}\to 22}\rangle$: decay of the bath particles to the FIMP (pFIMP).

We note here that the cBEQ as shown in Eq. (1) describes the WIMP-WIMP, or WIMP-FIMP, or FIMP-FIMP case for different strengths of the DM-SM interactions; $\langle\sigma v\rangle_{\mathrm{WIMP}} \sim 10^{-10}$ GeV^{-2}, whereas $\langle\sigma v\rangle_{\mathrm{FIMP}} \sim 10^{-20}$ GeV^{-2}. The other distinction lies in the initial conditions, for WIMP: $\mathrm{Y}_1|_{x\sim 0} = Y_1^{\mathrm{eq}} \sim x^{3/2}e^{-x}$, while for FIMP: $\mathrm{Y}_2|_{x\sim 0} = 0$. The pFIMP solution for DM_2 from the above cBEQ is obtained when

$$\langle\sigma v\rangle_{\mathrm{SM}\to 22} \ll \langle\sigma v\rangle_{11\to 22} \sim \langle\sigma v\rangle_{11\to \mathrm{SM}} \sim 10^{-10}\ \mathrm{GeV}^{-2}.$$

[1]The minimal version of such a framework appears in [46], where the fermion DM acts as the pFIMP, while the scalar acts as the WIMP. However, the model is ruled out by the present direct search bound.

We further note the discrepancy of a factor of 2 in Eq. (1), stemming from the symmetry factor in identical particle production for 2 as in the BEQ for Y_2, while that is absent in annihilation of 1 as for Y_1.

We would like to mention that the production of the pFIMP can occur from the decay of some heavy thermal bath particle. But for the pFIMP condition above to be met, the decay has to be suppressed as well (i.e., $\langle\Gamma_{\mathrm{SM}\to 22}\rangle \sim n^{\mathrm{eq}}_{\mathrm{SM}}\langle\sigma v\rangle_{\mathrm{SM}\to 22}$).

We further note that the cBEQ is written in terms of yields $\mathrm{Y}_{1,2} = \frac{n_{1,2}}{s}$, where s refers to the entropy density (per comoving volume) as

$$s = \frac{2\pi^2}{45} g^s_\star(T) T^3; \qquad g^s_\star(T) = \sum_k \mathcal{C}_k g_k \left(\frac{T_k}{T}\right)^3 \theta(T - m_k). \tag{2}$$

Here k runs over all particles, T_k is the temperature of particle k, g_k is its number of internal degrees of freedom, and $\mathcal{C}_k = 1(7/8)$ when k is a boson(fermion). We also define the Hubble parameter as

$$\mathcal{H}(T) = 1.66\sqrt{g^\rho_\star}\frac{T^2}{\mathrm{M_{pl}}}; \tag{3}$$

$$g^\rho_\star(T) = \sum_{i=\mathrm{bosons}} g_i \left(\frac{T_i}{T}\right)^4 + \frac{7}{8}\sum_{i=\mathrm{fermions}} g_i \left(\frac{T_i}{T}\right)^4. \tag{4}$$

We will assume the relativistic degrees of freedom (d.o.f.) $g^{\rho,s}_\star \approx 106.7$ to be approximately constant as the temperature during which the FIMP freezes in or the WIMP freezes out is rather high. Further, since the two DMs with different masses $m_{1,2}$ are involved, we define a common variable $x = \mu_{12}/T$, where $\mu_{12} = m_1 m_2/(m_1 + m_2)$ is the reduced mass of the system. This is possible as both the pFIMP and WIMP share the same temperature. With the redefined x we can write the equilibrium yield [2] as

$$Y^{\mathrm{eq}}_i(x) = \frac{45}{4\pi^4}\frac{g_i}{g^s_\star}\left(\frac{m_i}{\mu_{12}}x\right)^2 K_2\left(\frac{m_i}{\mu_{12}}x\right). \tag{5}$$

The expressions of thermal average of annihilation cross section is given by

$$\langle\sigma v_{12}\rangle = \frac{1}{8m_1^2 m_2^2 T}\frac{1}{K_2\left(\frac{m_1}{T}\right)K_2\left(\frac{m_2}{T}\right)} \times \int_{(m_1+m_2)^2}^{\infty} \sigma(s)(s-(m_1+m_2)^2)\sqrt{s}K_1\left(\frac{\sqrt{s}}{T}\right)ds, \tag{6}$$

where $v_{12} = (1/(E_1E_2))\sqrt{(p_1.p_2)^2 - m_1^2 m_2^2}$ denotes Möllar velocity, s denotes center-of-mass energy, and $m_{1,2}, E_{1,2}, p_{1,2}$ denote annihilating DM masses, energy, and momentum, respectively. K_i's denote the modified Bessel functions of second kind, of order i. We further note that the conversion from one DM species to the other are related by

$$\langle\sigma v\rangle_{11\to 22} = \langle\sigma v\rangle_{22\to 11}\left(\frac{Y^{\mathrm{eq}}_2}{Y^{\mathrm{eq}}_1}\right)^2. \tag{7}$$

This indicates that when the WIMP is heavier than the pFIMP, i.e., $m_1 > m_2$ (hierarchy 1), WIMP to pFIMP conversion is kinematically allowed, while the reverse process is Boltzmann suppressed by a factor $\sim e^{-2x\delta m}$, δm denoting the mass difference between the DMs. It is the other way around for $m_2 > m_1$ (hierarchy 2). This feature helps to distinguish the mass hierarchies in the pFIMP-WIMP model. The key features of pFIMP freeze-out are discussed in detail in [53], a summary of which is as follows:

(i) pFIMP freezes out together or before the WIMP, so the relic density of the pFIMP is always larger than the WIMP partner.[2] When the conversion cross section is of similar order to that of WIMP annihilation to the SM, both the pFIMP and WIMP share similar relic densities.
(ii) When the conversion rate is higher than the WIMP annihilation, the freeze-out and resultant relic density of the pFIMP remains constant in hierarchy 1, while the WIMP relic density becomes much smaller. In hierarchy 2, this is exactly the other way around. With larger conversion, the WIMP relic remains constant and the pFIMP relic drops sharply.
(iii) The mass splitting between the WIMP and pFIMP needs to be small ($\delta m \sim 10$ GeV, for $m_{\mathrm{DM}} \sim 100$ GeV) for achieving relic density and direct search allowed parameter space, unless we have resonance, coannihilation, semiannihilation, or some other special features of the conversion process.

B. pFIMP-SM interactions via WIMP loop

pFIMPs having feeble tree level interactions with the SM can interact via the WIMP loop. Such one loop interaction vertices are shown in Fig. 1. Here pFIMPs (on the right) are shown by black lines, WIMPs (in the loop) are denoted by red lines, SM particles (on the left of the interaction vertex) are shown by grey lines. As pFIMPs and WIMPs are stabilized by separate symmetries, the bath particles which complete the loop, as denoted by the teal color lines, transform suitably under both the symmetries. The dashed, solid, and wavy lines indicate scalar, fermion, and vector bosons for WIMPs (pFIMPs) and the vertices conserve spin, which in turn fixes the SM portal (Z, h).

[2]Recall that for thermal DM $\Omega h^2 \sim 1/\langle\sigma v\rangle$.

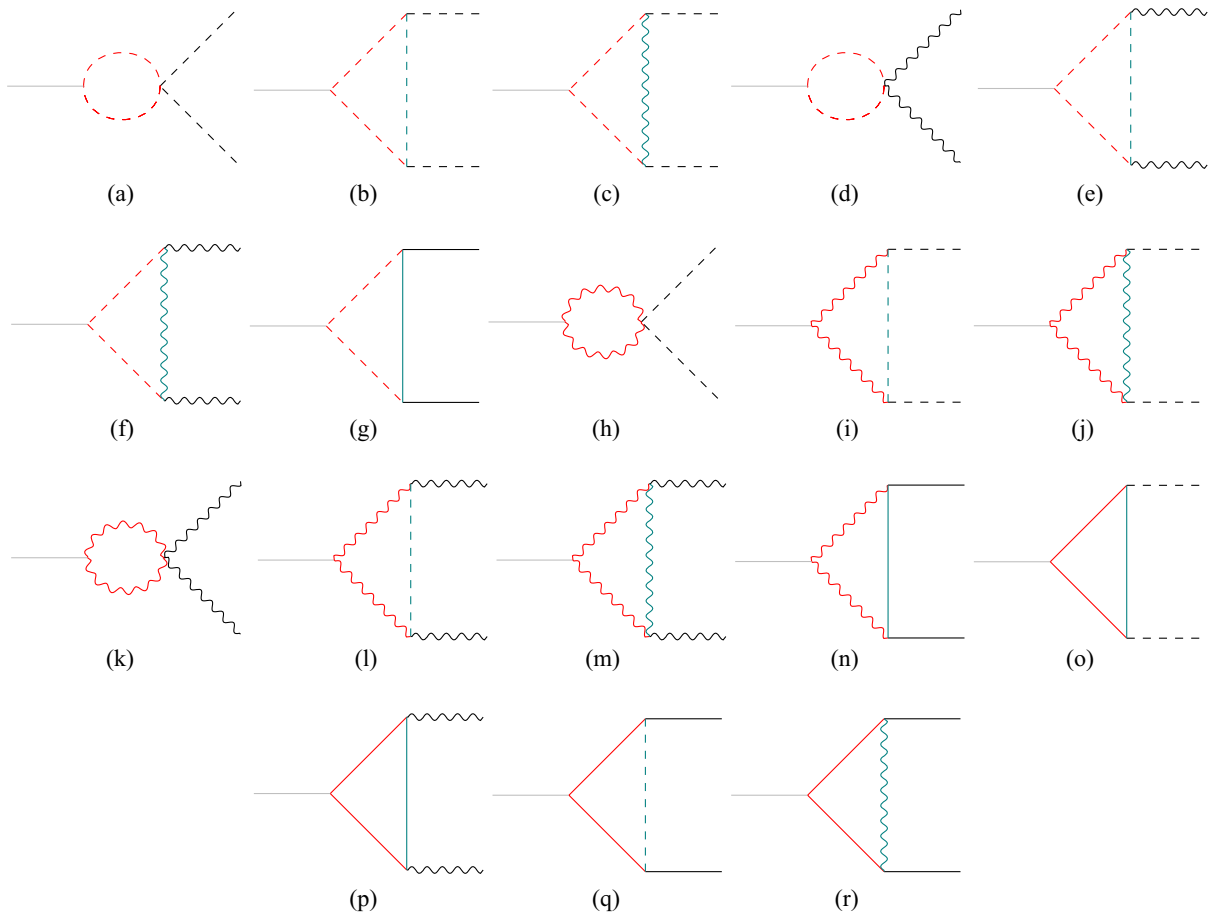

FIG. 1. Feynman diagrams (a–r) showing pFIMP (on the right denoted by black lines) interaction with the SM (Z, h) particles (on the left denoted by grey color lines) via WIMPs (in red) and heavy thermal bath particles (in teal color) in the loop. All possible interaction vertices having scalar (dashed), fermion (solid), and vector boson (wavy lines) WIMPs and pFIMPs transforming under $\mathbb{Z}_2 \otimes \mathbb{Z}_2'$ symmetries as in Table I have been considered.

In Table I, we have shown all possible renormalizable interactions between WIMPs and pFIMPs in a two component DM scenario stabilized by $\mathbb{Z}_2 \otimes \mathbb{Z}_2'$ symmetry for all combinations of scalar, fermion, and vector boson particles. These vertices generate the diagrams shown in Fig. 1. WIMPs are odd under $\mathbb{Z}_2$ and even under $\mathbb{Z}_2'$, while pFIMPs are odd under $\mathbb{Z}_2'$, and even under $\mathbb{Z}_2$. Particles denoted by prime $(\chi', \psi', \phi', X_\mu')$ are odd under both $\mathbb{Z}_2 \otimes \mathbb{Z}_2'$, which connect WIMP and pFIMP states as shown by the teal color lines in Fig. 1. This list excludes dark sector particles having nontrivial SM charges, more complicated spin configurations and higher order operators having mass dimension larger than 4. A short account of these models and their interactions are as follows:

(i) Figures 1(a)–1(c) correspond to the scenarios where both the WIMPs and pFIMPs are scalars. In Figs. 1(b) and 1(c), DMs are further connected by an extra heavy scalar (vector) bath particle shown in teal color. Corresponding WIMP-pFIMP interactions that generate these graphs are mentioned in Table I. For Fig. 1(c), other interaction terms apart from $(\partial^\mu \phi)\Phi X_\mu'$ like $(\partial^\mu X_\mu')\phi\Phi$ or $(\partial^\mu \Phi)\phi X_\mu'$ are also possible.

(ii) Figures 1(d)–1(f) depict scalar WIMPs and vector boson pFIMPs. Figures 1(e) [1(f)] requires a heavy scalar (vector boson) bath particle connecting them. See Table I for corresponding interaction terms. For Fig. 1(e), other terms like $\phi(\partial_\mu V^\mu)\phi'$, $\phi V^\mu(\partial_\mu \phi')$ are also possible apart from $(\partial_\mu \phi)V^\mu \phi'$ as in Table I.

(iii) Figure 1(g) represents interaction between a scalar WIMP and fermion pFIMP scenario. In this scenario an extra fermion bath particle is necessary for interaction. This model has been addressed before [46]. For all the scalar WIMP cases discussed so far, the interaction with the SM can be governed by the Higgs portal coupling $\phi^2 H^\dagger H$.

(iv) Figures 1(h)–1(j) correspond to vector boson WIMP and scalar pFIMP scenarios. Figures 1(i) [1(j)] requires extra scalar (vector boson) bath particles for the interaction, see Table I. For Fig. 1(i), an interaction term like $X^\mu(\partial_\mu \Phi)\phi'$ is also allowed. The WIMP-SM interaction for vector boson WIMPs can

TABLE I. Possible WIMP-pFIMP renormalizable interactions for real scalar, fermion, and vector boson particles [see the corresponding Feynman diagrams in Fig. 1] assuming $\mathbb{Z}_2 \otimes \mathbb{Z}_2'$ symmetries to stabilize both. Particles denoted by prime $(\chi', \psi', \phi', X'_\mu)$ are odd under both the $\mathbb{Z}_2$ symmetries, indicated by the teal color lines in Fig. 1, and connect WIMPs and pFIMPs. $\boldsymbol{\mu}$ represents a dimensionful coupling having one mass dimension.

	WIMP-pFIMP Model				
Scenarios	WIMP	pFIMP	Interaction terms	Relic	Detection possibility
(a)	Scalar(ϕ)	Scalar(Φ)	$\phi^2\Phi^2$	✓ [47,53]	✗
(b)	Scalar(ϕ)	Scalar(Φ)	$\boldsymbol{\mu}\phi\Phi\phi'$	✗	✗
(c)	Scalar(ϕ)	Scalar(Φ)	$(\partial^\mu\phi)\Phi X'_\mu$	✗	✗
(d)	Scalar(ϕ)	Vector(V)	$\phi^2 V^\mu V_\mu$	✗	✗
(e)	Scalar(ϕ)	Vector(V)	$(\partial_\mu\phi)V^\mu\phi'$	✗	✗
(f)	Scalar(ϕ)	Vector(V)	$\boldsymbol{\mu}\phi X^\mu X'_\mu$	✗	✗
(g)	Scalar(ϕ)	Fermion(χ)	$\bar{\chi}\chi'\phi$	✓ [46]	✓ [46]
(h)	Vector(X)	Scalar(Φ)	$X^\mu X_\mu\Phi^2$	✗	✗
(i)	Vector(X)	Scalar(Φ)	$X^\mu(\partial_\mu\phi')\Phi$	✗	✗
(j)	Vector(X)	Scalar(Φ)	$\boldsymbol{\mu}X^\mu X'_\mu\Phi$	✗	✗
(k)	Vector(X)	Vector(V)	$X^\mu X_\mu V^\nu V_\nu$	✗	✗
(l)	Vector(X)	Vector(V)	$\boldsymbol{\mu}X^\mu V_\mu\phi'$	✗	✗
(m)	Vector(X)	Vector(V)	$X^\mu V^\nu(\partial_\mu X'_\nu)$	✗	✗
(n)	Vector(X)	Fermion(χ)	$X_\mu\bar{\chi}\gamma^\mu\chi'$	✗	✗
(o)	Fermion(ψ)	Scalar(Φ)	$\bar{\psi}\psi'\Phi$	This work	This work
(p)	Fermion(ψ)	Vector(V)	$\bar{\psi}\gamma^\mu\psi' V_\mu$	✗	✗
(q)	Fermion(ψ)	Fermion(χ)	$\bar{\psi}\chi\phi'$	✗	✗
(r)	Fermion(ψ)	Fermion(χ)	$\bar{\psi}\gamma^\mu\chi X'_\mu$	✓ [48]	✗

be driven by $X^\mu X_\mu H^\dagger H$. Note further that we are ignoring the detailed possibility of an Abelian/non-Abelian gauge origin of the vector boson here.

(v) Figures 1(k)–1(m) correspond to a situation where both WIMPs and pFIMPs are vector bosons. The DMs are connected by a scalar [Fig. 1(l)] or a vector boson [Fig. 1(m)] bath particle as shown in the interaction vertices in Table I. Figure 1(m) can be generated by other interaction terms depending on the field derivative term, as argued before. The WIMP-SM interaction can also occur via Higgs portal as mentioned above. Figure 1(n) shows the possibility of vector boson WIMPs and fermion pFIMPs interacting with each other via another fermion bath particle as shown in teal color.

(vi) Finally, Figs. 1(o)–1(r) correspond to fermion-scalar, fermion-vector, and (fermion-fermion) WIMP-pFIMP setups. Figures 1(q) [1(r)] require scalar (vector boson) bath particles for interaction. Connection of the fermion WIMP to the SM can occur via effective operator term of the form $\bar{\psi}\psi H^\dagger H$ or via a Yukawa interaction involving a heavy fermion doublet like $\bar{\Psi}\psi H + \text{H.c.}$ We are going to elaborate upon Fig. 1(o) in a UV complete model next.

The right and cross signs in the relic and detection possibilities in Table I indicate whether such models have been studied before or not. We can see that amongst various possibilities mentioned WIMP-pFIMP phenomenology has been explored in a few cases, that too, without elaborating upon the characteristics of the pFIMP, its decoupling, and/or detectability. The scalar particle as both a pFIMP and WIMP has been explored in [47,53]. In [47], it was pointed out that when pFIMP couples to the SM via a scalar WIMP loop, the direct search detectability becomes difficult, however, in [53], it was shown that the direct search possibility emerges when the renormalization scale is chosen at the freeze-out temperature. We will elaborate more on this later. In [46], the fermion pFIMP was studied in a scalar-fermion set up as in Fig. 1(c), however, the resulting parameter space of this model is almost ruled out by the recent most direct search results. In [48], pFIMP phenomenon was discussed partially, but the detectability of the pFIMP via WIMP loop has been neglected.

III. AN EXAMPLE OF PFIMP-WIMP MODEL

Our focus will be now on a WIMP-pFIMP two component DM set up where the direct detection possibility of the pFIMP is achieved in next generation experiments. We will also make connections to the indirect detection prospects. The model consists of (i) a real scalar-singlet ϕ, which acts like the pFIMP and (ii) the lightest admixture of a vectorlike fermion doublet $\psi = (\psi^0\psi^-)^T$ [54,55] and a vectorlike singlet fermion ψ_1, which acts as WIMP DM.

TABLE II. Dark sector fields and their corresponding quantum numbers.

Dark fields	$SU(3)_c \times SU(2)_L \times U(1)_Y \times \mathbb{Z}_2 \times \mathbb{Z}'_2$				
$\psi = \binom{\psi^0}{\psi^-}$	1	2	−1	−	+
ψ_1	1	1	0	−	+
ψ_2	1	1	0	+	−
ϕ	1	1	0	−	−

We additionally introduce another vectorlike singlet fermion ψ_2, which acts as a messenger between the two DM sectors. Stability of both the DM components is ensured by a $\mathbb{Z}_2 \otimes \mathbb{Z}'_2$ symmetry. The charges of all the relevant fields are given in Table II.

Abiding by the symmetry charges, the corresponding Lagrangian is given by

$$\mathcal{L} = \mathcal{L}_{\rm SM} + \mathcal{L}_{\rm Scalar} + \mathcal{L}_{\rm VF}, \tag{8}$$

where

$$\mathcal{L}_{\rm Scalar} = \frac{1}{2}|\partial_\mu \phi|^2 - \frac{1}{2}\mathfrak{m}_\phi^2 \phi^2 - \frac{1}{4!}\lambda_\phi \phi^4 - \frac{1}{2}\lambda_{\phi H}\phi^2 H^\dagger H, \tag{9}$$

and

$$\begin{aligned}\mathcal{L}_{\rm VF} = {} & \bar{\psi}\left[i\gamma^\mu\left(\partial_\mu + ig\frac{\sigma^a}{2}W_\mu^a + ig'\frac{Y}{2}B_\mu\right) - m_\psi\right]\psi \\ & + \sum_{\alpha=1,2}\bar{\psi}_\alpha(i\gamma^\mu\partial_\mu - m_{\psi_\alpha})\psi_\alpha \\ & - (Y_1\bar{\psi}\tilde{H}\psi_1 + Y_2\bar{\psi}_2\psi_1\phi + \text{H.c.}).\end{aligned} \tag{10}$$

After EWSB, the SM Higgs H acquires vacuum expectation value $v = 246$ GeV, so that in unitarity gauge we can write, $H = (0\,\frac{1}{\sqrt{2}}(v+h))^T$. Then the physical mass term of ϕ can be written as $m_\phi^2 = \mathfrak{m}_\phi^2 + \frac{1}{2}\lambda_{\phi H}v^2$. ϕ is a stable DM candidate and serves as the pFIMP component when $\lambda_{\phi H} \to 0$, and conversion to the fermion DM is substantial via large Y_2. From Eq. (10), it is straightforward to calculate the mass terms for the vectorlike fermions. The mass eigenstates (χ_1, χ_2) can be obtained via diagonalization of the fermion mass matrix through a unitary transformation from the flavor basis (ψ_1, ψ^0),

$$-\mathcal{L}_{\rm mass} = m_{\chi_1}\bar{\chi}_1\chi_1 + m_{\chi_2}\bar{\chi}_2\chi_2 + m_\psi\psi^+\psi^-, \tag{11}$$

where

$$\chi_1 = \cos\theta\psi_1 + \sin\theta\psi^0, \tag{12}$$

$$\chi_2 = -\sin\theta\psi_1 + \cos\theta\psi^0, \tag{13}$$

$$m_{\chi_1} = \sin^2\theta m_\psi + \cos^2\theta m_{\psi_1} + \frac{Y_1 v}{\sqrt{2}}\sin 2\theta, \tag{14}$$

$$m_{\chi_2} = \cos^2\theta m_\psi + \sin^2\theta m_{\psi_1} - \frac{Y_1 v}{\sqrt{2}}\sin 2\theta. \tag{15}$$

The mixing angle θ can be written as

$$\tan 2\theta = \frac{\sqrt{2}Y_1 v}{m_{\psi_1} - m_\psi}. \tag{16}$$

Using Eq. (16), we can easily write,

$$Y_1 = \frac{\sin 2\theta}{\sqrt{2}v}(m_{\chi_1} - m_{\chi_2}), \tag{17}$$

$$m_\psi = m_{\chi_1}\sin^2\theta + m_{\chi_2}\cos^2\theta, \tag{18}$$

$$m_{\psi_1} = m_{\chi_1}\cos^2\theta + m_{\chi_2}\sin^2\theta. \tag{19}$$

m_ψ denotes the mass of the charged components of the doublet $\psi^\pm$. The independent parameters of our model are

$$\{m_{\chi_1}, m_{\chi_2}, m_{\psi_2}, m_\phi, \sin\theta, Y_2, \lambda_{\phi H}\}.$$

χ_1 being the lightest neutral fermion, serves as the WIMP DM component. Note here that χ_1 having gauge interaction with the SM via doublet component ψ^0 cannot be a pFIMP. In general, any DM having gauge coupling with the SM can never be a pFIMP. The mass difference between χ_1 and the second lightest neutral fermion χ_2, denoted as $\Delta m = m_{\chi_2} - m_{\chi_1}$ serves as an important parameter that controls the coannihilation process and the resulting WIMP relic density. We would like to comment here that the model is perfectly valid as a two component DM scenario without the presence of ψ_2, but cannot provide an interaction between ϕ and χ_1. Then it can serve best as a WIMP-WIMP (in the limit of sizeable $\lambda_{\phi H}$) or a WIMP-FIMP (with $\lambda_{\phi H} \to 0$) model. The presence of ψ_2 provides the much needed Yukawa interaction Y_2 between the DM components and allows the model to be explored in pFIMP(ϕ)-WIMP(χ) combination. We can now also correlate with Fig. 1(o): χ_1 is the fermion WIMP in the red color, ϕ is the pFIMP in the dashed black line, and ψ_2 is the bath particle connecting them as shown in the teal color. Mass difference between χ_1 and ϕ is denoted in the following text by $\delta m = m_\phi - m_{\chi_1}$ and is also highly constrained by pFIMP freeze-out to yield under abundance.

Following the DM-DM interaction term $Y_2\bar{\psi}_1\psi_2\phi$, we will be interested in the region where $m_{\psi_2} > m_{\chi_1} + m_\phi$, so

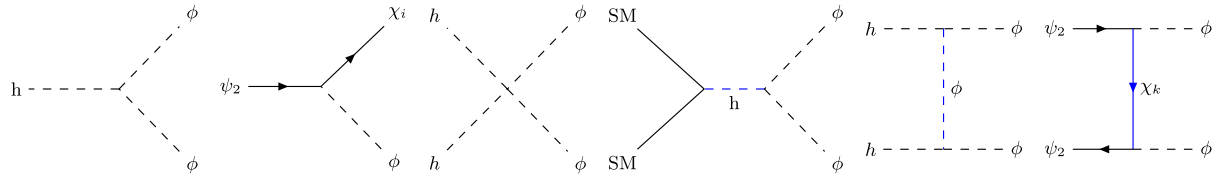

FIG. 2. Feynman diagrams for pFIMP ϕ production from thermal bath $\{i, k = 1, 2\}$.

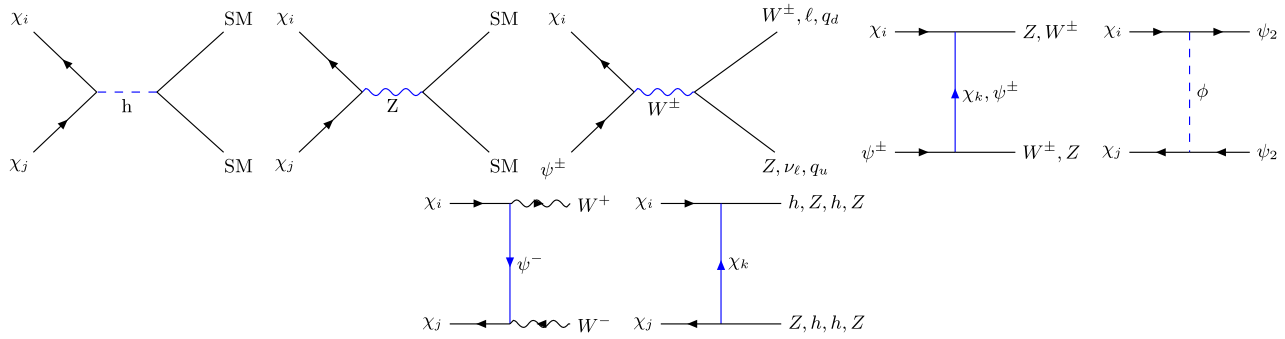

FIG. 3. Feynman diagrams for the possible annihilation and coannihilation channels of WIMP χ_1 $\{i, j, k = 1, 2\}$.

that ψ_2 can decay to χ_1 and ϕ. The relevant Feynman diagrams for pFIMP production, (co)-annihilation of WIMPs, WIMP-pFIMP conversions and semiconversion are shown in Figs. 2–4, respectively. In particular, note the presence of a semiconversion channel $\chi_1\psi_2 \to h\phi$ in Fig. 4, which also helps in evading the stringent pFIMP mass constraint on δm. We choose a tiny $\lambda_{\phi H} \sim 10^{-12}$ so that ϕ does not possess a direct SM interaction and behaves as a pFIMP, it also helps us evade the upper bound on Higgs invisible branching ratio (BR) $\mathrm{BR}(h \to \text{invisible}) < 19\%$ at 2σ [56] as well as the direct detection constraints to explore the mass range below the Higgs resonance $m_\phi < (m_h/2)$ as well. It is worthy, however, to mention that the mediator ψ_2 generates ϕ-Higgs portal as a counterterm of the loop mediated interaction (see Appendix C for details) and allows for the direct search of pFIMPs. For details on Higgs and Z invisible decay width and resulting constraints, see Appendix A. Notably, a bound from the large electron positron (LEP) experiments on the charged fermion masses [57–61] $\gtrsim$103.5 GeV also discard the low DM mass region of the relic density allowed parameter space, following Eqs. (17)–(19).

Before moving further, we would like to make a couple of comments. The very idea that pFIMP-WIMP conversion governs the pFIMP freeze-out distinguishes a scalar pFIMP in a two component scalar DM model from that described here. Also the detectability of pFIMPs relies on the loop and the particles involved therein, which provides a distinct possibility for the model at hand, as we elaborate here. To sum it up, it is not only the pFIMP particle itself, but its WIMP partner, and its interaction with the WIMP holds the key for phenomenological outcome of the two component DM setup.

IV. DARK MATTER PHENOMENOLOGY

Having discussed the model, we will focus on the DM phenomenology highlighting the pFIMP freeze-out behavior followed up by the scan of the allowed parameter space.

A. Coupled Boltzmann equations and relic density

After considering all the relevant processes, the cBEQ's involving the fermion WIMP (χ_1) and scalar pFIMP (ϕ) turn out to be [62–66]

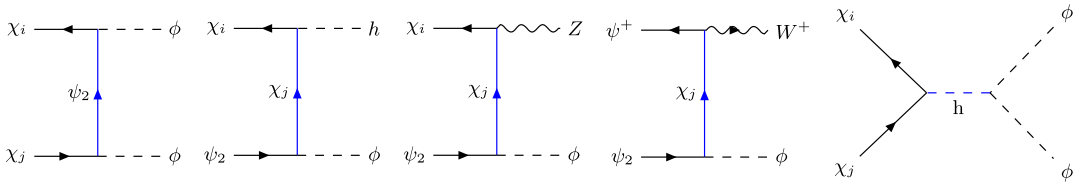

FIG. 4. Feynman diagrams contributing to WIMP-pFIMP conversion $\{i, j = 1, 2\}$.

$$\frac{dY_\chi}{dx} = -\frac{2\pi^2 M_{\rm pl}}{45\times 1.66}\frac{g_\star^s}{\sqrt{g_\star^\rho}}\frac{\mu_{\chi_1\phi}}{x^2}\Big[\langle\sigma v\rangle^{\rm eff}_{\rm SM}(Y_\chi^2 - Y_\chi^{\rm eq^2}) + \langle\sigma v\rangle^{\rm eff}_{\phi}\left(Y_\chi^2 - Y_\chi^{\rm eq^2}\frac{Y_\phi^2}{Y_\phi^{\rm eq^2}}\right)$$
$$+ \langle\sigma v\rangle^{\rm eff}_{\psi_2}\left(Y_\chi^2 - Y_\chi^{\rm eq^2}\frac{Y_{\psi_2}^2}{Y_{\psi_2}^{\rm eq^2}}\right) + (\langle\sigma v\rangle^{\rm eff}_{\chi_1\bar\psi_2\to h\phi} + \langle\sigma v\rangle^{\rm eff}_{\psi^-\bar\psi_2\to W^-\phi})\left(Y_{\psi_2}Y_\chi - Y^{\rm eq}_{\psi_2}Y^{\rm eq}_\chi\frac{Y_\phi}{Y^{\rm eq}_\phi}\right)$$
$$+ \langle\sigma v\rangle^{\rm eff}_{\chi_1\bar\psi_2\to Z\phi}\left(Y_{\psi_2}Y_\chi - Y^{\rm eq}_{\psi_2}Y^{\rm eq}_\chi\frac{Y_\phi}{Y^{\rm eq}_\phi}\right)\Big] + \frac{M_{\rm pl}}{1.66\sqrt{g_\star^\rho}}\frac{x}{\mu^2_{\chi_1\phi}}\langle\Gamma\rangle^{\rm eff}_{\psi_2\to\chi_1\phi}\left(Y_{\psi_2} - Y^{\rm eq}_{\psi_2}\frac{Y_\phi}{Y^{\rm eq}_\phi}\frac{Y_\chi}{Y^{\rm eq}_\chi}\right), \tag{20}$$

$$\frac{dY_\phi}{dx} = \frac{M_{\rm pl}}{1.66\times\sqrt{g_\star^\rho}}\frac{x}{\mu^2_{\chi_1\phi}}\left[2\langle\Gamma\rangle_{h\to\phi\phi}\left(Y_h^{\rm eq} - Y_h^{\rm eq}\frac{Y_\phi^2}{Y_\phi^{\rm eq^2}}\right) + \langle\Gamma\rangle^{\rm eff}_{\psi_2\to\chi_1\phi}\left(Y_{\psi_2} - Y^{\rm eq}_{\psi_2}\frac{Y_\phi}{Y^{\rm eq}_\phi}\frac{Y_\chi}{Y^{\rm eq}_\chi}\right)\right]$$
$$+ \frac{2\pi^2 M_{\rm pl}}{45\times 1.66}\frac{g_\star^s}{\sqrt{g_\star^\rho}}\frac{\mu_{\chi_1\phi}}{x^2}\Big[2\langle\sigma v\rangle_{\rm SM\,SM\to\phi\phi}\left(Y^{\rm eq^2}_{\rm SM} - Y^{\rm eq^2}_{\rm SM}\frac{Y_\phi^2}{Y_\phi^{\rm eq^2}}\right)$$
$$+ 2\langle\sigma v\rangle_{\psi_2\bar\psi_2\to\phi\phi}\left(Y_{\psi_2}^2 - Y_{\psi_2}^{\rm eq^2}\frac{Y_\phi^2}{Y_\phi^{\rm eq^2}}\right) + (\langle\sigma v\rangle^{\rm eff}_{\chi_1\bar\psi_2\to h\phi} + \langle\sigma v\rangle^{\rm eff}_{\psi^-\bar\psi_2\to W^-\phi})\left(Y_{\psi_2}Y_\chi - Y^{\rm eq}_{\psi_2}Y^{\rm eq}_\chi\frac{Y_\phi}{Y^{\rm eq}_\phi}\right)$$
$$+ \langle\sigma v\rangle^{\rm eff}_{\chi_1\bar\psi_2\to Z\phi}\left(Y_{\psi_2}Y_\chi - Y^{\rm eq}_{\psi_2}Y^{\rm eq}_\chi\frac{Y_\phi}{Y^{\rm eq}_\phi}\right) + 2\langle\sigma v\rangle^{\rm eff}_{\phi}\left(Y_\chi^2 - Y_\chi^{\rm eq^2}\frac{Y_\phi^2}{Y_\phi^{\rm eq^2}}\right)\Big]. \tag{21}$$

In Eqs. (20) and (21), Y_ϕ is the pFIMP yield, and Y_χ is the total WIMP yield (assimilating contributions from the heavy dark sector particles),

$$Y_\chi = \sum_i Y_{\chi_i}, \quad \chi_i = \{\chi_1, \bar\chi_1, \chi_2, \bar\chi_2, \psi^\pm\}. \tag{22}$$

It is worth reminding that all the unstable heavy states such as $\psi^\pm$, χ_2 take part in coannihilation processes when in equilibrium. Legitimately, $\chi_i, \psi^\pm$ are in equilibrium by rapid annihilations into bath particles. This is also true for ψ_2, via processes as mentioned in Eq. (24) for sizeable $Y_2 \gtrsim 10^{-2}$ when $\langle\Gamma_{\psi_2}\rangle/\mathcal{H}(T) > 1$ as shown in Fig. 5(a), so that their number densities can be chosen to be the equilibrium number density ($Y^{\rm eq}$) during the DM saturation epoch.[3] We have also shown the variation of $\langle\Gamma_\phi\rangle/\mathcal{H}(T)$ as a function of T in Fig. 5(b) for different values of Y_2, where $\langle\Gamma_\phi\rangle$ is given by Eq. (23). The chemical equilibrium is achieved for $Y_2 \gtrsim 10^{-4}$. Note that

$$\langle\Gamma_\phi\rangle = 2\sum_{i=1,2}(\langle\sigma v\rangle_{\phi\chi_i\to h\psi_2} + \langle\sigma v\rangle_{\phi\chi_i\to Z\psi_2})n^{\rm eq}_{\chi_i}$$
$$+ 2\langle\sigma v\rangle_{\phi\psi^-\to W^-\psi_2}n^{\rm eq}_{\psi^-} + \langle\sigma v\rangle_{\phi\phi\to\rm SM\,SM}n^{\rm eq}_\phi, \tag{23}$$

and

$$\langle\Gamma_{\psi_2}\rangle = (\langle\sigma v\rangle_{\psi_2\bar\chi_1\to h\phi} + \langle\sigma v\rangle_{\psi_2\bar\chi_1\to Z\phi})n^{\rm eq}_{\chi_1} + (\langle\sigma v\rangle_{\psi_2\bar\chi_2\to h\phi}$$
$$+ \langle\sigma v\rangle_{\psi_2\bar\chi_2\to Z\phi})n^{\rm eq}_{\chi_2} + \langle\sigma v\rangle_{\psi_2\psi^+\to W^+\phi}n^{\rm eq}_{\psi^+}$$
$$+ [\langle\sigma v\rangle_{\psi\bar\psi_2\to hh} + \langle\sigma v\rangle_{\psi\bar\psi_2\to hZ} + \langle\sigma v\rangle_{\psi\bar\psi_2\to ZZ}$$
$$+ \langle\sigma v\rangle_{\psi\bar\psi_2\to W^+W^-} + \langle\sigma v\rangle_{\psi\bar\psi_2\to\ell\bar\ell} + \langle\sigma v\rangle_{\psi\bar\psi_2\to q\bar q}]n^{\rm eq}_{\psi_2}. \tag{24}$$

After the freeze-out, they eventually decay to the lightest stable DM χ_1, contributing to its relic density. This issue is addressed via "effective" annihilation cross section to SM $\langle\sigma v\rangle^{\rm eff}$ and effective decay width $\langle\Gamma\rangle^{\rm eff}$ (see [67] and Appendix B for details), where all possible SM final states such as $h, W^\pm, Z, \ell, q$ are considered. Also note that in Eqs. (20) and (21), $M_{\rm pl} = 1.22091\times 10^{19}$ GeV represents Planck mass, and $g_\star^s \simeq g_\star^\rho \approx 106.7$ denotes effective massless degrees of freedom. The common variable $x = \frac{\mu_{\chi_1\phi}}{T}$ written in terms of the reduced mass $\mu_{\chi_1\phi} = (\frac{1}{m_{\chi_1}} + \frac{1}{m_\phi})^{-1}$ caters to the two component DM system in equilibrium. The dark sector particles follow the nonrelativistic equilibrium distribution given by

$$Y^{\rm eq}_\phi = \frac{45}{4\pi^4}\frac{g_\phi}{g_\star^s}\left(x\frac{m_\phi}{\mu_{\chi_1\phi}}\right)^2 K_2\left(x\frac{m_\phi}{\mu_{\chi_1\phi}}\right), \tag{25}$$

[3]Two points to note here; one, the equilibration is easier when ψ_2 is part of a doublet via gauge interactions. Second, it is not necessary to have ψ_2 in equilibrium for the WIMP (χ)-pFIMP (ϕ) exchange process to be substantial (as required here), although several other terms of the BEQs (20) and (21) will change to yield a different allowed parameter space.

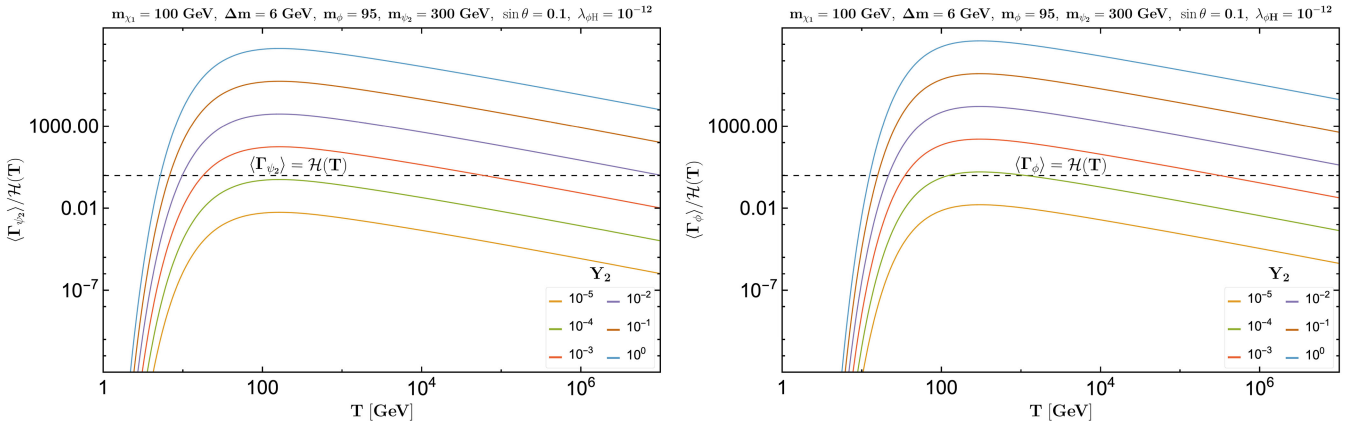

FIG. 5. Variation of $\langle\Gamma_{\psi_2}\rangle/\mathcal{H}(T)$ as a function of T (GeV) in (a) and $(\langle\Gamma_\phi\rangle/\mathcal{H}(T))$ in (b) for different values of Yukawa couplings Y_2 as shown by different colored lines.

$$Y_\chi^{\rm eq} = \frac{45}{4\pi^4}\sum_i \frac{g_i}{g_\star^s}\left(x\frac{m_i}{\mu_{\chi_1\phi}}\right)^2 K_2\left(x\frac{m_i}{\mu_{\chi_1\phi}}\right). \quad (26)$$

In writing the Eqs. (20) and (21), we also have used [62]

$$\frac{n_i}{n} \approx \frac{n_i^{\rm eq}}{n^{\rm eq}}, \qquad n^{\rm eq} = \sum_i n_i^{\rm eq} = \frac{T}{2\pi^2}\sum_i g_i m_i^2 K_2\left(\frac{m_i}{T}\right). \quad (27)$$

In the above, T represents the common temperature that DM particles possess, and K_2 represents modified Bessel function of second order. Note further that the scalar DM ϕ is assumed out-of-equilibrium initially due to tiny $\lambda_{\phi H}$, but reaches thermal equilibrium and becomes a pFIMP by large conversion from/to WIMP via $\chi_1\chi_1 \to \phi\phi$. A symmetry factor of 2 applies for ϕ [see Eq. (21)]. A subsequent solution of the cBEQ provides relic density of the DM species by

$$\Omega_{\rm DM}h^2 = 2.744\times 10^8\left(m_{\chi_1}Y_\chi\left[\frac{m_{\chi_1}}{\mu_{\chi_1\phi}}x_\infty\right] + m_\phi Y_\phi\left[\frac{m_\phi}{\mu_{\chi_1\phi}}x_\infty\right]\right), \quad (28)$$

where x_∞ corresponds to the present time/temperature.

The solutions of cBEQs are presented in terms of DM yield as a function of x in Figs. 6(a) and 6(b) for two different mass hierarchies. Light brown and violet dotted lines represent a pure FIMP situation with

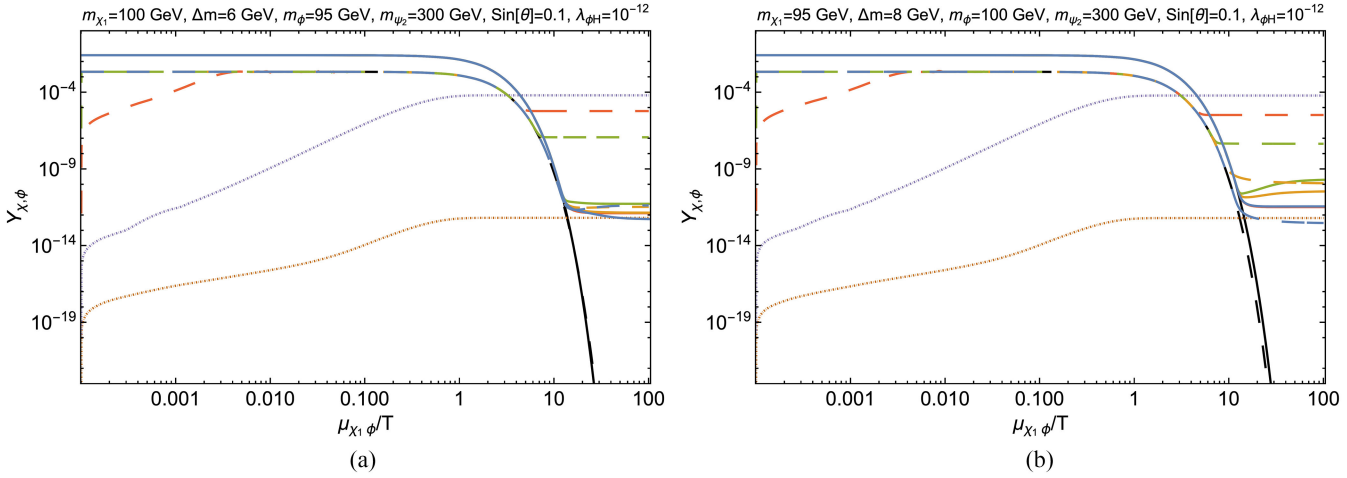

FIG. 6. (a) Shows the variation of yield (Y) of WIMPs (thick lines), pure FIMPs (dotted lines), and pFIMPs (dashed lines) as a function of x where light brown, violet, red, green, yellow, and deep blue lines correspond to different values of Y_2: $\{10^{-12}, 10^{-8}, 10^{-4}, 10^{-2}, 1, 2\}$, respectively, for $m_{\chi_1} > m_\phi$. (b) Shows the same for $m_{\chi_1} < m_\phi$ with different values of Yukawa coupling Y_2: $\{10^{-12}, 10^{-8}, 10^{-4}, 10^{-2}, 10^{-1}, 0.5\}$ represented by light brown, violet, red, green, yellow, and deep blue lines, respectively. The black thick and dashed lines show the equilibrium distribution of WIMPs and pFIMPs, respectively. Other parameters kept fixed are mentioned in the figure caption.

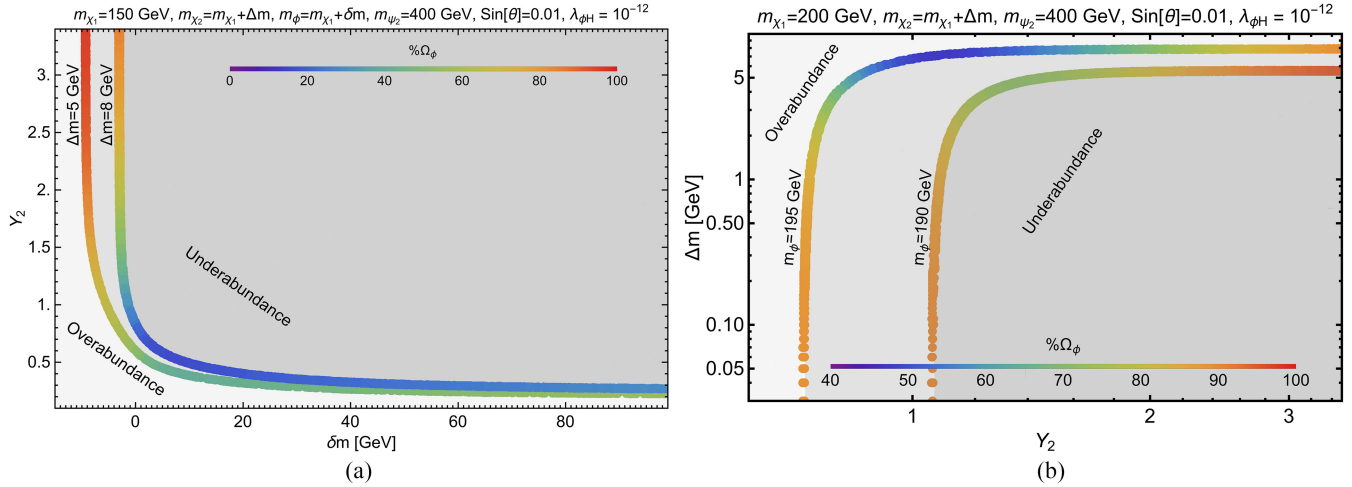

FIG. 7. Parameter space allowed by the observed relic ($0.1188 \leq \Omega_{\rm DM}h^2 \leq 0.1212$) in (a) δm-Y_2 plane and (b) Y_2-Δm plane. In both the figures percentage contribution of the pFIMP (Ω_ϕ) is shown in the color bar. Parameters kept fixed are mentioned in the figure heading.

$Y_2 = \{10^{-12}, 10^{-8}\}$, respectively, wherein the DM freezes. For $Y_2 = 10^{-8}$, with larger conversion from WIMP to FIMP, the FIMP yield increases. However, with Y_2 increasing further ($Y_2 \gtrsim 10^{-3}$), the FIMP thermalizes to the equilibrium number density via the conversion process and enters into the pFIMP regime (red, green, yellow, and deep blue dashed lines) to freeze-out subsequently. The red dashed curve(s), in particular, show how the pFIMP enters into the thermal bath. The pFIMP thermal equilibration is already checked in Fig. 5(b). The change in the WIMP or pFIMP number density/freeze-out point depends on the mass hierarchy as well as on the conversion cross section. Here in both the plots, while the pFIMP relic density decreases with larger Y_2 (via larger conversion cross section), notice that the WIMP relic density does not change much. This is because the WIMP annihilation plus coannihilation still remains larger than that of the conversion cross section for the chosen parameters. For detailed pFIMP dynamics see [53].

In Fig. 7(a), we show the relic density allowed parameter space of the model in δm-Y_2 plane, where the total relic density adds to the observed one ($\Omega h^2 = 0.1200 \pm 0.0012$) [1] for fixed $\{m_\chi, \Delta m, m_{\psi_2}, \sin\theta\}$ as indicated in the figure caption. Two sets of Δm are chosen. Smaller Δm enhances coannihilation of the WIMP and thus reduces the contribution to the total relic. It is clear from the percentage contribution of the pFIMP (ϕ) to the total DM relic as shown in the color axis. Overabundant and underabundant regions fall below and above the correct choice of Y_2 quite expectedly owing to the inverse dependence of relic density to the conversion cross sections, as indicated. Recall that $\delta m = m_\phi - m_{\chi_1}$ represents the mass difference between the pFIMP and WIMP. The parameter space can be divided into two regions: (i) $\delta m > 0$, i.e., the pFIMP is heavier than the WIMP; (ii) $\delta m < 0$, when the WIMP is heavier than the pFIMP. The results are different for these cases. When $\delta m > 0$, there is a mild dependence on δm, as the conversion process does not depend heavily on it and contribution to the WIMP relic density is small, thus pFIMP contribution remains in the 20% ballpark with almost no change in Y_2. However, when $\delta m < 0$, the WIMP has an additional depletion channel, and its relic density decreases with larger conversion to the pFIMP with larger splitting, in turn the pFIMP relic enhances significantly, which requires it to be adjusted by having larger Y_2 to keep the total relic within the observed one. In Fig. 7(b), we show the relic density allowed parameter space in Y_2-Δm plane. As mentioned earlier, here, Δm is the mass difference between the second lightest fermionic dark sector particle χ_2 and the WIMP DM χ_1. With larger Y_2, and therefore larger $\chi_1 \to \phi$ conversion, the coannihilation effect is required to reduce with larger Δm and the relative contribution of ϕ to the total relic density increases. We further see that a maximum of $\Delta m \lesssim 10$ GeV is possible for pFIMP ϕ to saturate the most of DM abundance. The parameters kept fixed are mentioned in the figure caption, and the two choices of m_ϕ used for the scan are mentioned in the plot.

B. Direct detection prospect

Now we delve into the direct search prospect of the two component DMs, which is our key focus in this study. First, we will briefly discuss the direct detection of the WIMP and then explore the pFIMP case in detail.

1. Direct detection of the WIMP

In this model, the spin-independent direct detection cross section for WIMP χ_1 ($\sigma^{\rm SI}_{\chi_1 N}$) gets major contribution from Z and Higgs-mediated t-channel diagrams (Fig. 8),

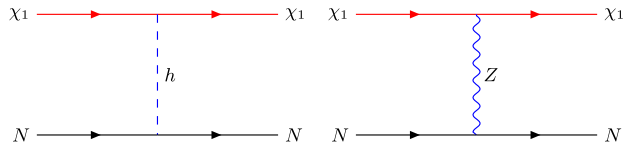

FIG. 8. The Feynman diagrams for the direct detection of WIMP (χ_1).

and therefore, the singlet-doublet mixing parameter $\sin\theta$ plays an important role, apart from the DM mass m_{χ_1}. The direct search prospect of this WIMP is similar to that in [55,68]. The Z mediated contribution is required to be small to abide by the nonobservation of a spin-independent direct search of the DM. This is possible when the singlet-doublet mixing ($\sin\theta$) is small, since the effective coupling involved in the Z mediated vertex is $\lambda_{Z\bar{\chi}_1\chi_1} = \frac{m_Z}{v}\sin^2\theta$, whereas the effective Higgs coupling is $\lambda_{h\bar{\chi}_1\chi_1} = -\frac{Y_1}{\sqrt{2}}\sin 2\theta$.

In Figs. 9(a) and 9(b) we show the effective spin-independent direct detection cross section ($\sigma^{\rm eff}_{\chi_1}$) of the WIMP-like fermion DM χ_1 as a function of its mass (m_{χ_1}) for two different mass hierarchies. We also show the limits from existing direct search data along with future sensitivities. The effective direct search cross section for the individual DM components are defined [69] as follows:

$$\sigma^{\rm eff}_{\chi_1} = \frac{\Omega_{\chi_1}}{\Omega_{\chi_1}+\Omega_\phi}\sigma^{\rm SI}_{\chi_1 N}; \qquad \sigma^{\rm eff}_{\phi} = \frac{\Omega_{\phi}}{\Omega_{\chi_1}+\Omega_\phi}\sigma^{\rm SI}_{\phi N}. \quad (29)$$

In both the Figs. 9(a) and 9(b) $\sin\theta$ is shown in the color bar. It is clear that with increasing $\sin\theta$, i.e., with more doublet contribution, the direct detection cross section for χ_1 increases. One finds in Fig. 9(a), when $m_{\chi_1} \lesssim 100$ GeV, only in the vicinity of Z resonance, we get points allowed by the relic density, but disfavored from direct search data. The points allowed by the direct search data requires $m_\chi \gtrsim 100$ GeV with $\sin\theta \lesssim 0.1$. In the reverse hierarchy [Fig. 9(b)], the Z-resonance region is not particularly distinct. The reason behind this is the following. When $m_{\chi_1} > m_\phi$, the conversion channel from χ_1 to ϕ is open, which helps χ_1 to deplete its number density considerably and become underabundant, whereas when $m_{\chi_1} < m_\phi$, this conversion is kinematically disfavored, and therefore, the underabundance for χ_1 is achieved primarily near Z resonance. Here too, small mass difference between χ_1 and χ_2 can facilitate coannihilation, and there exists a possibility of underabundance with the appropriate choice of Δm. The black dots over the rainbow points are disfavored from the LEP limit on charged fermion masses. The same appears in other parameter space scans. The detailed calculation of the direct detection cross section of the WIMP can be found in Appendix D.

2. Direct detection of the pFIMP

The FIMP having negligible coupling with SM states is difficult to probe in direct search experiments. The pFIMP on the other hand, despite having negligible couplings to the SM, has a prospect of being detected at direct search experiments via substantial coupling with the WIMP. As discussed in Sec. II B, the pFIMP coupling to the SM occurs via the WIMP-loop, which can have a non-negligible contribution to the elastic scattering between the pFIMP and detector nucleon.

In Fig. 10, we show the diagrams which contribute to the direct search cross section of pFIMP (ϕ) in our model. The diagram [Fig. 10 (left)] involving the Higgs portal coupling

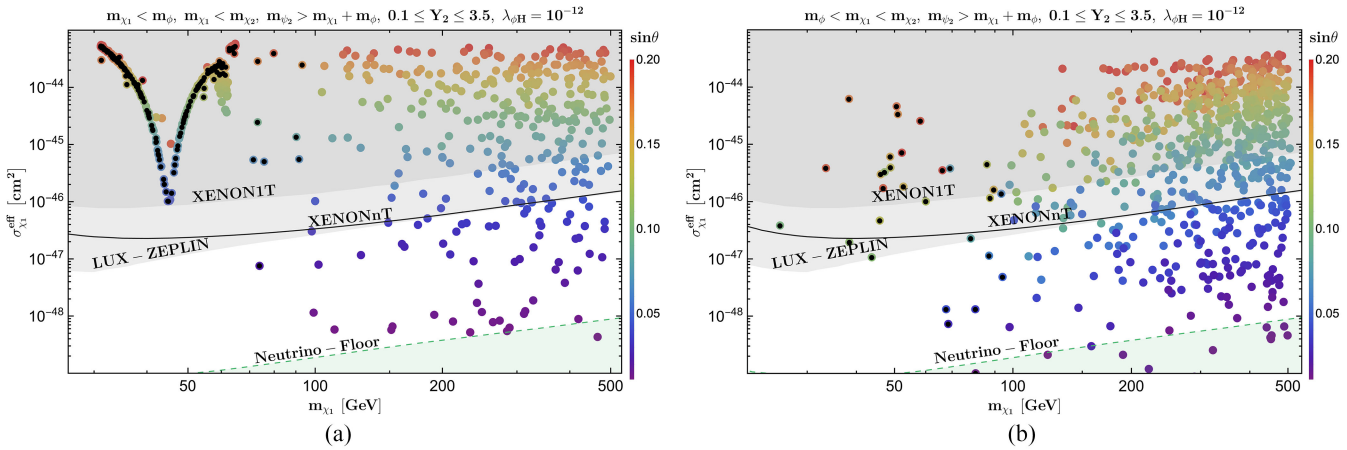

FIG. 9. Effective spin-independent direct detection cross section ($\sigma^{\rm eff}_{\chi_1}$) for WIMP χ_1 for (a) $m_{\chi_1} < m_\phi$ and (b) $m_{\chi_1} > m_\phi$. All the points satisfy the present DM relic density bound $0.1188 \le \Omega_{\chi_1}h^2 + \Omega_\phi h^2 \le 0.1212$ via the combined contribution of both DMs. $\sin\theta$ is shown as the color axis in both the figures. Other parameters kept fixed are shown in the figure heading. The limits from XENON1T, LUX-ZEPLIN data and future sensitivities from XENONnT and the neutrino floor are shown. Black dotted points are excluded by the LEP bound on the charged fermion masses.

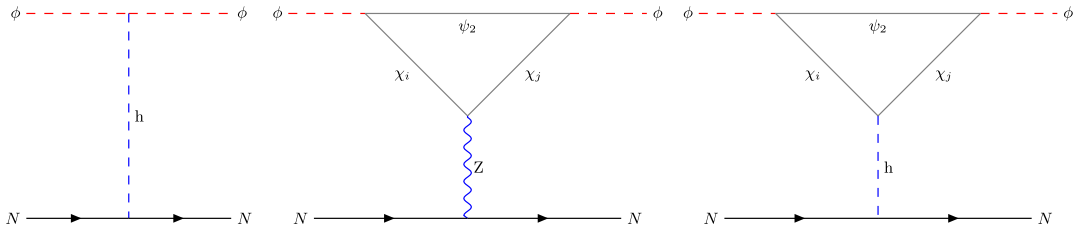

FIG. 10. Feynman diagrams for direct detection of pFIMP ϕ, via tree level Higgs mediation (left), one-loop Z mediation (middle) and one-loop Higgs mediation (right).

of the pFIMP, contributes negligibly to the total amplitude with $\lambda_{\phi H} \sim 10^{-12}$. Figure 10 (middle) shows the WIMP-loop induced contribution with a t-channel Z mediator, whereas Fig. 10 (right) shows the same with t-channel Higgs mediation.

The coupling that plays a crucial role in determining the loop amplitude is the WIMP-pFIMP coupling (Yukawa coupling Y_2), which was also a key parameter in governing the pFIMP dynamics. On the other hand, one has to also remember that the loop contributions are also a direct consequence of the singlet-doublet mixing in our model. In the absence of mixing, the loop contribution to pFIMP-nucleon interaction vanishes. Therefore, not only the Yukawa coupling Y_2, but also the Yukawa coupling Y_1 is crucial in this context. In addition, the mixing term is directly proportional to the mass difference between the WIMP and the second lightest dark sector particle $(m_{\chi_2} - m_{\chi_1})$, as we have seen in Eq. (17). The smaller the mass difference, the weaker the detectability is of the pFIMP at direct detection experiments. Similar to the WIMP case, here too the Higgs mediated diagram contributes much more compared to the Z-mediated case, thanks to the small $\sin\theta$ limit that we need to abide by. For an order-of-magnitude estimate of the Higgs and Z mediated contributions, one can see Figs. 19 and 21 in Appendix C. We would like to emphasize here that we get an advantage by choosing a fermionic WIMP candidate over a scalar. It was shown in [47] that the pFIMP, in a two-component scalar DM model, will have negligible contribution to the direct detection as the scalar loop amplitude vanishes at the low transfer momentum limit (unless the WIMP is a warm DM in the KeV mass range). Although that issue can be alleviated if we choose the renormalization scale at the DM mass scale, however, the scale dependence remains. This is not the case with the fermion WIMP loop, see the detailed calculations in Appendix C. Herein lies a very important motivation behind choosing the model. The detailed calculation of direct detection cross section of the pFIMP is done in Appendix D, which we use for the parameter space scan discussed next.

In Fig. 11, we present the effective spin-independent direct detection cross section ($\sigma_\phi^{\rm eff}$) of the pFIMP ϕ as a function of its mass (m_ϕ) for two different mass hierarchies. The definition of $\sigma_\phi^{\rm eff}$ follows from Eq. (29). As the major contribution to $\sigma_\phi^{\rm eff}$ comes from the fermion-loop induced diagrams (Fig. 10), the parameters Δm, Y_2, and $\sin\theta$ play a crucial role. In order to achieve a considerable direct

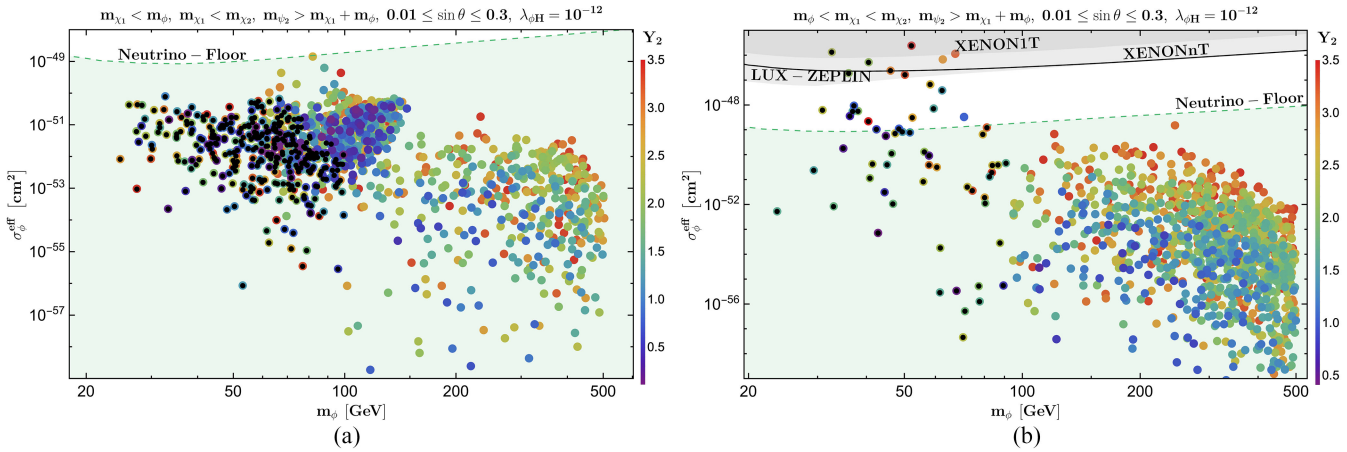

FIG. 11. Effective spin-independent direct detection cross section ($\sigma_\phi^{\rm eff}$) for pFIMP ϕ for (a) $m_{\chi_1} < m_\phi$ and (b) $m_{\chi_1} > m_\phi$. All the points satisfy the present DM relic density bound $0.1188 \leq \Omega_{\chi_1} h^2 + \Omega_\phi h^2 \leq 0.1212$ via the combined contribution of both DMs. Y_2 is shown as the color axis in both figures. Other parameters kept fixed are shown in the figure heading. The limits from XENON1T, LUX-ZEPLIN data, and future sensitivities from XENONnT and the neutrino floor are shown. Black dotted points are excluded by the LEP bound on the charged fermion masses.

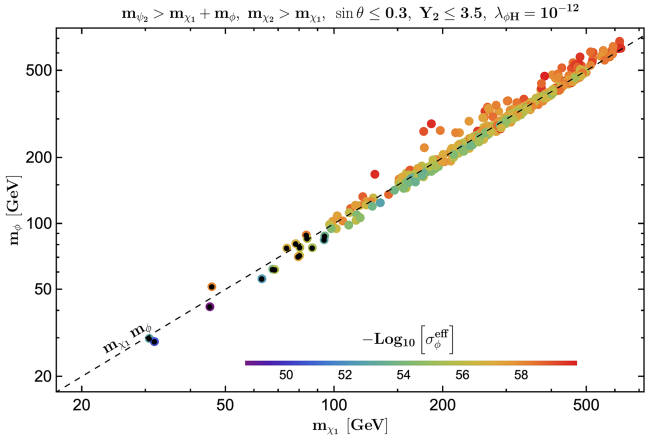

FIG. 12. Allowed parameter space in m_{χ_1}-m_ϕ plane, which respect the present observed relic density as well as have sensitivities for future direct detection experiments beyond the LUX-ZEPLIN bound. The color axis represents the effective spin-independent pFIMP-nucleon scattering cross section, σ_ϕ^{eff} in cm^2 in log scale. Black dotted points are excluded by the LEP bound on the charged fermion masses.

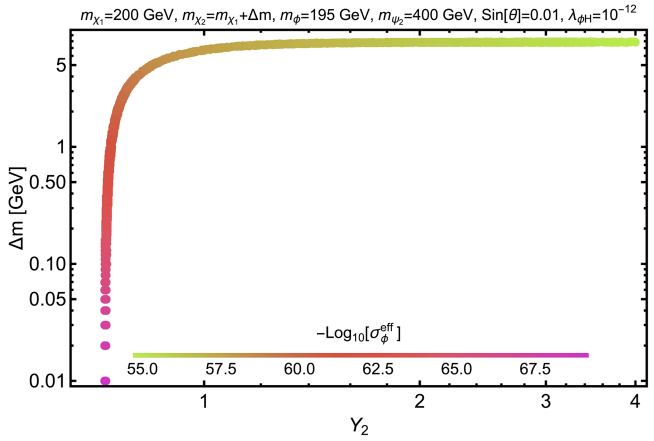

FIG. 13. Parameter space allowed by observed relic density and direct search constraints in Y_2-Δm plane, where the spin-independent effective DM-nucleon elastic scattering cross section of scalar DM (σ_ϕ^{eff} in cm^2) is shown as the color axis in log scale.

detection cross section, a large mass splitting Δm is desirable, as already pointed out. On the other hand, large Δm means absence of coannihilation and therefore overabundance of χ_1. This situation is evident in Fig. 11(a), where the parameter space allowed by observed relic density implies direct detection cross section for the pFIMP not only lies below the existing direct search limits, but a large part remains within the neutrino floor sensitivity. This tension is relaxed when $m_{\chi_1} > m_\phi$, since in this case the conversion channel from χ_1 to ϕ becomes kinematically favored, and the underabundance of χ_1 is possible even with moderate/large Δm. This in turn ensures a moderate direct search cross section (10^{-49}–10^{-47}) for the pFIMP with mass $\lesssim$100 GeV, which can be probed in the next generation direct detection experiments like Xenon-nT (projected limit 10^{-49} cm^2), as shown in Fig. 11(b). Hereby, we draw a crucial inference that $m_{\chi_1} > m_\phi$ is more favorable for the direct detection of pFIMPs, as compared to the inverse hierarchy in this specific model.

Having discussed the individual aspects of WIMP and pFIMP direct detection, we would also like to make a connection between the two. In Fig. 12, we have shown the allowed parameter space, which respect the present relic density and direct detection (LUX-ZEPLIN) bound in m_{χ_1}-m_ϕ plane. The color axis represents the effective spin-independent pFIMP-nucleon scattering cross section, $\sigma_\phi^{\text{eff}}(\text{cm}^2)$ in log scale. One can, firstly, observe that the allowed region lies in the vicinity of $m_{\chi_1} = m_\phi$ line in accordance with the pFIMP dynamics [53]. When $m_{\chi_1} > m_\phi$, χ_1 to ϕ conversion is significant, reducing the WIMP contribution and enhancing ϕ contribution to the total relic, and therefore, the effective σ_ϕ^{eff} increases too.

Now see the red points above the $m_{\chi_1} = m_\phi$ line, i.e., the opposite hierarchy ($m_{\chi_1} < m_\phi$). One can notice the presence of larger $\delta m \sim 100$ GeV points for this hierarchy, which was absent in the other hierarchy in accordance with Fig. 7. In addition, if χ_1 is in the Z resonance, then the underabundance of χ_1 becomes further enhanced, and it becomes easier to achieve large Δm and, consequently, large direct detection cross section for the pFIMP (blue points in the vicinity of Z resonance in Fig. 12). For the inverse hierarchy, on the other hand, the underabundance of the WIMP is solely dependent on its coannihilation, and therefore, large Δm values are disfavored, resulting in small direct detection cross section for the pFIMP. We have checked that even with χ_1 in the vicinity Z resonance, the dependence on coannihilation is not relaxed, and therefore, direct detection cross section for the pFIMP remains below the neutrino floor for almost the entire parameter space.

In Fig. 13, we show the relic density and direct search allowed points in Y_2-Δm plane, with the color axis denoting the direct detection cross section of the pFIMP ϕ in log scale. The shape of the curve is exactly similar to that of Fig. 7(b), dictated by the relic density constraint, which limits $\Delta m \lesssim 10$ GeV to assimilate the effect of annihilation/coannihilation of the WIMP. Larger Δm imply enhanced contribution from the fermion loop (see Fig. 10) resulting in larger direct detection cross section for the pFIMP, evident from the transition in color in Fig. 13. Increasing Y_2 is also crucial in obtaining enhanced direct search cross section σ_ϕ^{eff}, also apparent from the color of the curve.

C. Indirect detection possibility

Similar to the direct detection prospects of pFIMPs, one can obtain indirect signal evidence of pFIMPs, analyzing the photon flux [70] in the existing and future indirect

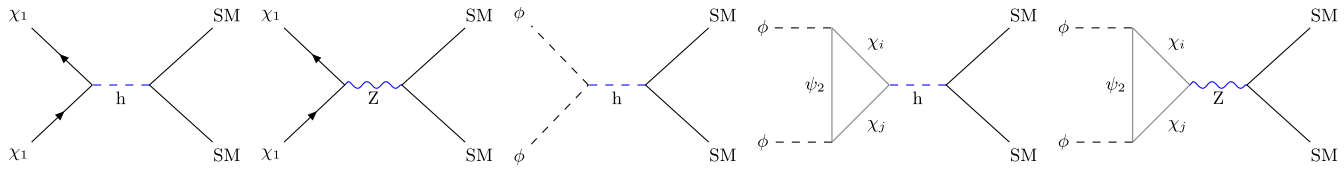

FIG. 14. The tree-level (left) and one-loop (right) Feynman diagrams for the indirect detection of WIMP (χ_1) and pFIMP (ϕ).

detection experiments such as *Fermi* Large Area Telescope (LAT) [71], Super Kamio-Kande [72], high energy stereoscopic system [73], IceCube [74–76], etc. We have considered the recent data for DM annihilation channels to $b\bar{b}$, $\tau^+\tau^-$, and W^+W^- from various experiments and study their effect on our model parameter space. The strongest bounds come from the $b\bar{b}$ annihilation channel. The effective annihilation cross section of a DM pair to $b\bar{b}$ final state in a two-component DM setup is given by [77,78]

$$\langle\sigma v\rangle^{\rm ID}_{\rm DM\,DM\to b\bar{b}} = \frac{\Omega^2_{\rm DM}}{(\Omega_{\chi_1}+\Omega_{\phi})^2}\langle\sigma v\rangle_{\rm DM\,DM\to b\bar{b}}. \tag{30}$$

In the above, DM notation indicates WIMP (χ_1) or pFIMP (ϕ).

In Fig. 14, we show the processes that contribute to the aforementioned annihilation channels for both WIMPs and pFIMPs. Note that the tree-level Higgs mediated channel for pFIMP annihilation turns negligible with $\lambda_{\phi H}\to 0$, while the WIMP-loop induced diagrams dominantly contribute to pFIMP annihilation, similar to the direct search case.

In Fig. 15, we plot $\langle\sigma v\rangle^{\rm ID}_{\rm DM\,DM\to b\bar{b}}$ as a function of DM mass for WIMPs [Fig. 15(a)] and pFIMPs [Fig. 15(b)]. The color axis denotes the effective direct detection cross section for pFIMP ($\sigma^{\rm eff}_{\phi}$). All the points in both plots satisfy the observed relic and LUX-ZEPLIN bound. It is evident from the figures that the entire parameter space is allowed by indirect bound from *Fermi* LAT (black dashed line) and can be probed in future experiments. Interestingly, the region that is most sensitive to the future indirect detection experiments lies in the vicinity of Z resonance. The same points also produce maximum direct search cross section for the pFIMP [dark blue points in Fig. 15(b)] and thereby yield best discovery potential.

D. Collider constraints and prospects at LHC

The WIMP sector of the model having additional particles transforming under the SM gauge group naturally have collider detectability as well as constraints from the existing data [55,80,81]. The hardest limit appears on the model from the LEP exclusion [57] of not observing a singly charged fermion beyond the SM, resulting in $m_{\psi^\pm}\gtrsim 103.5$ GeV. The ALTAS [82,83] and CMS [84] experiments at the LHC have looked for DM signals in opposite sign dileptons (OSD) + jets + $\not{E}_T$ missing transverse energy (MET) final state and nonobservation of any excess puts a limit on our model that produces such a signal. In our model, the corresponding signal process is predominantly generated by the Drell-Yan production of the charged fermion pair, subsequently decaying via off-shell $W^\pm$ as shown in Fig. 16(a). In Fig. 17, we show the LHC constraints in the plane of charged lepton mass and DM

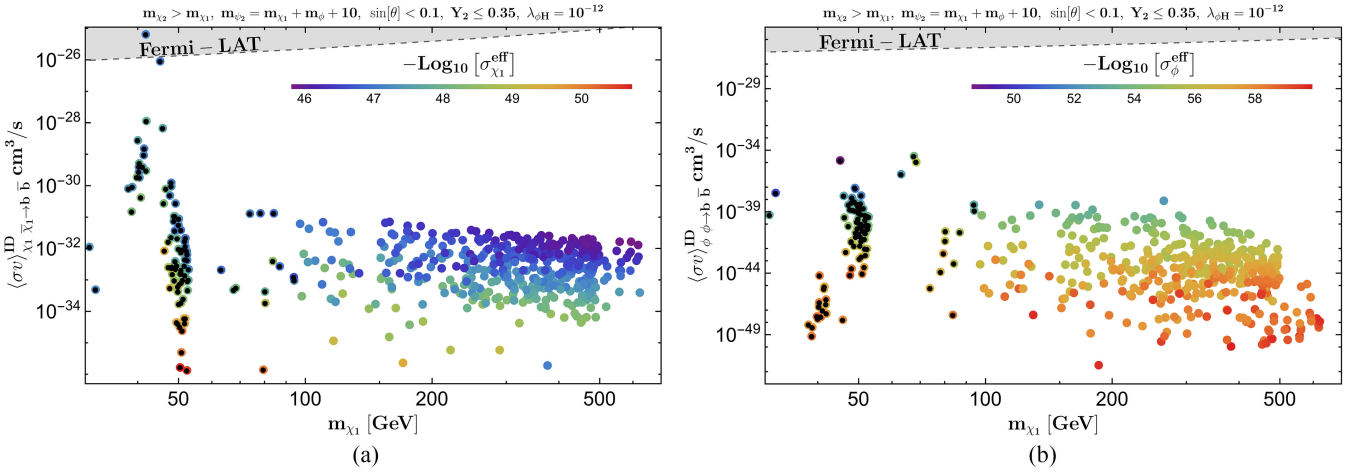

FIG. 15. DM annihilation cross section to $b\bar{b}$, $\langle\sigma v\rangle^{\rm ID}_{\chi_1\bar{\chi}_1\to b\bar{b}}$ (a), and $\langle\sigma v\rangle^{\rm ID}_{\phi\phi\to b\bar{b}}$ (b) as a function of DM mass. The color axis denotes effective direct detection cross section for pFIMP ($\sigma^{\rm eff}_{\phi}$). All points in $\sigma^{\rm ID}$-m_{χ_1} plane satisfy observed relic and LUX-ZEPLIN bound for both WIMPs and pFIMPs. The gray shaded region is excluded by DM annihilation to $b\bar{b}$ search at *Fermi* LAT [71,79] and H.E.S.S [73] data. Black dotted points are excluded by the LEP bound.

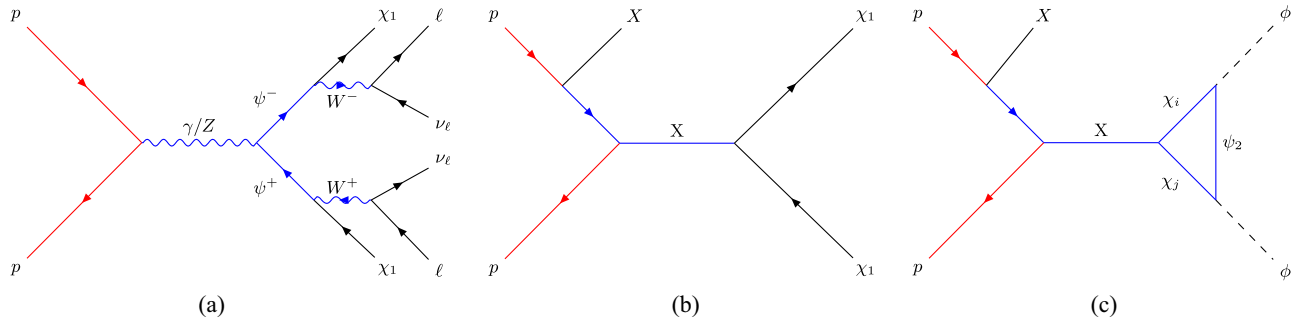

FIG. 16. Feynman diagrams showing $pp \to \psi^+\psi^-$ production and subsequent decays to opposite sign dilepton ($\ell^+\ell^- + \not{E}_T$) events (a), mono-$X + \not{E}_T$ signal for the WIMP (b) and the pFIMP (c); where $X =$ jet, γ, h, Z and $i = 1, 2$.

mass. This limit stems from the search for supersymmetric chargino, where the lightest neutralino serves as cold DM (both in gaugino-dominated regions), giving rise to OSD plus MET signal. One can see from here that large mass difference between the DM candidate and charged fermions are disallowed by the experimental data, i.e., the on-shell production of $W^{\pm}$ from the charged fermion decay is crucial for the parameter point to be sensitive to the experimental data. However, as we have discussed, in detail, in the small $\sin\theta$ limit, the requirement of adequate coannihilation makes the DM and charged fermion masses almost degenerate, see the maroon points that come from our model checked against the experimental constraints in Fig. 17. Therefore, the parameter space of our model, relevant from the DM constraints are allowed by the ATLAS and CMS bounds. It is interesting to note further that, only in the Z resonance region, the requirement for degenerate DM masses with its charged/neutral partners get relaxed, where a large mass gap becomes allowed from relic density constraints. Therefore, some of these points, where DM mass lies in the resonance region, can possess $\psi^{\pm} > 103.5$ GeV and survive all the experimental constraints (see Figs. 11 and 15). Apart from the OSD final state, the WIMP can be produced via several other channels like $\chi_2\chi_2$, $\chi_2\psi^{\pm}$ and their subsequent decays to produce $(1\ell, 2\ell, 3\ell, 4\ell)$ signals [55,80,81] in association with MET.

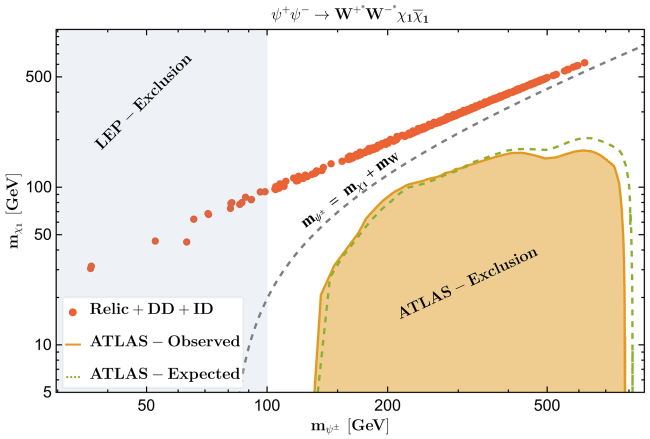

FIG. 17. WIMP masses $\gtrsim$103 GeV are allowed by ATLAS [82,83] and LEP [57] observed chargino signal.

On the other hand, the pFIMP can only be produced via the WIMP loop, yielding a mono-X ($X = j, \gamma, Z, W, h$) signal predominantly via initial state radiation, see Fig. 16(c). The WIMP of this specific model (or any other model) will always be able to produce the same mono-X signal [see Fig. 16(b)] and the WIMP cross section is larger than the pFIMP one, as the latter is always loop suppressed. Therefore, $\not{E}_T$ peak produced by the pFIMP will possibly be submerged into that of the WIMP, as the mass difference between them is not large. Note here that the distinguishability of the peaks in $\not{E}_T$ distribution heavily depends on the mass separation [50]. The pFIMP signal can possibly be distinguished from the WIMP partner, if the MET peak is separated due to different effective Lorentz structures for the production [51]. We will elaborate on this possibility concerning pFIMP production in a separate publication. We present the signal cross sections in Table III at some typical benchmark points for illustration. This indicates that the possibility of pFIMP detection of this model at the LHC is rather bleak.

V. SUMMARY AND CONCLUSIONS

We focused on a two-component DM scenario involving a thermal WIMP and a FIMP having negligible interaction with the SM. When the interaction between the WIMP and FIMP becomes of weak interaction strength, the FIMP thermalizes and freezes-out similar to the WIMP. Such DM candidates can be called pFIMPs, and we explored various aspects of this mechanism in our earlier work [53] in a model independent manner. In this work, we focus on a specific two component DM model to analyze the parameter space in the WIMP-pFIMP limit.

A crucial aspect of this work is to explore the possibility of detection of pFIMPs in direct and indirect search experiments. It is well known that a FIMP having tiny coupling to SM states evades both present and future (projected) direct detection bounds. However, the pFIMP, aided by its significant interaction with the WIMP, can have considerable DM-nucleon cross sections at the direct search

TABLE III. Relic density, direct search, and collider signal cross sections at some benchmark points for the two-component fermion-scalar model. All the masses are in the units of GeV. The last two columns depict the WIMP and pFIMP production cross section at the LHC via gluon fusion yielding mono-jet + $\not{E}_T$ in the final state at $\sqrt{s} = 14$ TeV. The OSD + MET final state cross section is estimated only via $\psi^+\psi^-$ production and cascade decay.

										$p-p$ collision (fb)		
										WIMP		pFIMP
m_{χ_1}	m_{χ_2}	m_ϕ	m_{ψ_2}	$\sin\theta$	Y_2	$\Omega_{\chi_1}h^2$	$\Omega_\phi h^2$	$\sigma^{\text{eff}}_{\chi_1}[\text{cm}^2]$	$\sigma^{\text{eff}}_{\phi}[\text{cm}^2]$	OSD + $\not{E}_T$	mono-jet + $\not{E}_T$	mono-jet + $\not{E}_T$
98.0	104.7	94.8	202.8	0.02	2.44	0.0092	0.1115	6.30×10^{-49}	1.40×10^{-55}	93.3	2.21×10^{-4}	1.49×10^{-9}
250.3	253.9	242.9	1121.2	0.04	1.61	0.0423	0.0783	2.27×10^{-47}	1.96×10^{-58}	3.67	1.38×10^{-4}	9.16×10^{-12}
456.1	461.4	454.7	920.8	0.02	2.43	0.0954	0.0258	2.11×10^{-48}	1.09×10^{-58}	0.312	8.42×10^{-7}	1.26×10^{-11}

experiments. Although, the pFIMP has no direct connection to the SM, it can produce WIMP-loop induced amplitudes, which can bring the pFIMP under future experimental sensitivities. Having identified all such one-loop possibilities with scalar, fermion, and vector boson particles as WIMPs and pFIMPs, we choose a specific model which is likely to provide a considerable direct and indirect search sensitivity for the pFIMP. It is important to note that pFIMP detectability depends heavily on its WIMP partner, not only due to its presence in the loop induced graphs for the pFIMP interacting with the SM, but also due to the fact that the underabundant region allowed for the pFIMP depends crucially on the WIMP annihilation/coannihilation channels. We focus on these two aspects of pFIMP dynamics in this model dependent study.

The model we chose to illustrate consists of a fermion WIMP which is an admixture of a singlet and a doublet. The pFIMP is a scalar singlet having negligible Higgs portal interaction and a substantial WIMP-pFIMP conversion via Yukawa interaction. Both possibilities like the fermionic WIMP and scalar WIMP at individual levels have been studied before, but the pFIMP phenomenology and the detectability that we analyse here is new in the literature. We have scanned the parameter space of our model and identified the region which is most sensitive to both direct and indirect search experiments. We found that one specific mass hierarchy with heavier WIMP is favored for direct detection. On the other hand, a large mass splitting between the WIMP and the second lightest dark sector particle is required for better pFIMP direct search. This is achieved when the WIMP mass lies in the vicinity of the Z-resonance region. Although the low WIMP mass region is strongly constrained from the LEP data as well as as from the LHC bound, allowed parameter space points are left in the Z-resonance region, albeit fine-tuned. Importantly, the WIMP being a fermion in this model, also helps to generate a significant loop-induced amplitude. We must note that our model is just one example that is conducive for pFIMP detectability, while there exists a plethora of possibilities as outlined in the beginning of this work.

Collider searches for the WIMP component of this model have been discussed in the literature. The WIMP sector of this model can produce a multilepton signal plus MET, thanks to the presence of a doublet. The limits from the current data leave a large allowed parameter space of the model for signal discovery at the future sensitivities of LHC. The pFIMP, on the other hand, can only be produced via WIMP loop and yield mono-X ($X = j, \gamma, Z, W, h$) signal via initial state radiation. WIMPs can also produce the same signal, but with a larger cross section. So the pFIMP signal is likely to be submerged into the WIMP signal, having little or no consequence in the final state event numbers or distributions in this scenario.

The other crucial feature that the WIMP-pFIMP setup provides, after addressing the correct relic density, is to have a small mass difference between the two DM components, around $\lesssim$10 GeV, which, however, gets relaxed to some extent in one particular hierarchy of this model. But broadly we expect two DM signals (either in direct or in collider searches) in the same mass range. While this is very predictive on the one hand, disentangling them may be challenging. We plan to address these issues in a future analysis.

ACKNOWLEDGMENTS

S. B. and J. L. acknowledge the Grant No. CRG/2019/004078 from SERB, Government of India. D. P. thanks University Grants Commission for senior research fellowship and Heptagon, IITG for useful discussions.

APPENDIX A: HIGGS AND Z INVISIBLE DECAY WIDTHS

The observed (expected) upper limit on the invisible branching fraction of the Higgs boson at 95% confidence level [85,86] having the total decay width of 125.1 GeV Higgs given by $3.2^{+2.8}_{-2.2}$ MeV [87] is

$$\mathcal{B}_{h\to\text{invisible}} < \begin{cases} 0.145(0.103) & (\text{ATLAS}) \\ 0.18(0.10) & (\text{CMS}). \end{cases} \tag{A1}$$

In this model, the invisible branching ratio comes from Higgs decay to both the WIMP and pFIMP given by

$$\Gamma_{h\to\phi\phi} = \frac{\mathbb{L}_h^2}{32\pi m_h}\left(1-4\frac{m_\phi^2}{m_h^2}\right)^{1/2}\Theta[m_h-2m_\phi], \tag{A2}$$

$$\Gamma_{h\to\chi_1\bar{\chi}_1} = \frac{\sin^4 2\theta}{32\pi v^2} m_h (m_{\chi_1}-m_{\chi_2})^2\left(1-4\frac{m_{\chi_1}^2}{m_h^2}\right)^{3/2} \Theta[m_h-2m_{\chi_1}]. \tag{A3}$$

In the above, $\mathbb{L}_h$ is one-loop corrected $h\to\phi\phi$ vertex as elaborated later.

The recent invisible decay width bound on the Z boson comes from various experiments like [88]

$$\Gamma_{Z\to\text{invisible}} < \begin{cases} 523\pm 16\ \text{MeV} & \text{(CMS)} \\ 503\pm 16\ \text{MeV} & \text{(LEPComb)} \\ 498\pm 17\ \text{MeV} & \text{(L3)}. \end{cases} \tag{A4}$$

Invisible Z boson decay can have contributions from both WIMPs and pFIMPs, given by

$$\Gamma_{Z\to\phi\phi} = \frac{\mathbb{L}_Z^2 m_Z}{16\pi}\left(1-4\frac{m_\phi^2}{m_Z^2}\right)^{3/2}\Theta[m_Z-2m_\phi], \tag{A5}$$

$$\Gamma_{Z\to\chi_1\bar{\chi}_1} = \frac{m_Z^3\sin^4\theta\sin^4\theta_w}{12\pi v^2}\left(1+2\frac{m_{\chi_1}^2}{m_Z^2}\right)\left(1-4\frac{m_{\chi_1}^2}{m_Z^2}\right)^{1/2} \Theta[m_Z-2m_{\chi_1}]. \tag{A6}$$

Here $\mathbb{L}_Z$ is one-loop corrected $Z\to\phi\phi$ vertex. The explicit expressions for $\mathbb{L}_h$ and $\mathbb{L}_Z$ will be given in Appendix C. If DM masses are below $m_h/2(m_Z/2)$, then it is severely constrained by the invisible Higgs and Z decay constraints.

APPENDIX B: BEQ WITH COANNIHILATION IN WIMP-PFIMP FRAMEWORK

Let us consider n_i dark sector particles have the same Z_2 symmetry, masses m_i (m_1 being the mass of DM), and internal d.o.f. g_i. The evolution of the number density n_i of particle i can be written as

$$\dot{n}_i + 3Hn_i = -\sum_j \langle\sigma v\rangle_{ij\to\text{SM}}(n_i n_j - n_i^{\text{eq}} n_j^{\text{eq}}). \tag{B1}$$

Since all the dark sector particles with $i>1$ will eventually decay to the stable DM candidate after their respective freeze-outs, the total DM density will be the result of the combined yield of all the dark sector particles. Therefore, its final abundance (n) can be described by the sum of the density of all the dark sector particles that transform under the same Z_2 symmetry,

$$n = \sum_i n_i. \tag{B2}$$

The corresponding evolution equation for n can be written as follows [62,67]:

$$\dot{n} = -3Hn - \sum_{i,j}\langle\sigma v\rangle_{ij\to\text{SM}}(n_i n_j - n_i^{\text{eq}} n_j^{\text{eq}}). \tag{B3}$$

In the above, we have assumed that n_i dark sector particles are initially in the thermal bath with the SM, and n_i^{eq} denotes the equilibrium number density. Using $\frac{n_i}{n} = \frac{n_i^{\text{eq}}}{n^{\text{eq}}}$, Eq. (B3) becomes

$$\dot{n} + 3Hn = -\sum_{ij}\langle\sigma v\rangle_{ij\to\text{SM}}\left(n_i^{\text{eq}}\frac{n}{n^{\text{eq}}} n_j^{\text{eq}}\frac{n}{n^{\text{eq}}} - n_i^{\text{eq}} n_j^{\text{eq}}\right) = -\langle\sigma v\rangle_{\text{SM}}^{\text{eff}}(n^2 - n^{\text{eq}^2}), \tag{B4}$$

where

$$\langle\sigma v\rangle^{\text{eff}} = \sum_{i,j}\langle\sigma v\rangle_{ij}\frac{n_i^{\text{eq}} n_j^{\text{eq}}}{n_{\text{eq}}^2} \quad \text{and} \quad n^{\text{eq}} = \sum_i n_i^{\text{eq}}. \tag{B5}$$

Following Eq. (B5), it is straightforward to calculate the $\langle\sigma v\rangle^{\text{eff}}$ for all possible channels relevant for our case as in Eqs. (20) and (21),

$$\langle\Gamma\rangle_{\psi_2\to\chi_1\phi}^{\text{eff}} = \sum_i \langle\Gamma\rangle_{\psi_2\to i\phi}, \tag{B6}$$

$$\langle\sigma v\rangle_{\chi_1\bar{\psi}_2\to h\phi}^{\text{eff}} = \left[\sum\nolimits_i g_i m_i^2 K_2\left(\frac{m_i}{T}\right)\right]^{-1}\sum_i \langle\sigma v\rangle_{i\bar{\psi}_2\to h\phi} g_i m_i^2 K_2\left(\frac{m_i}{T}\right), \tag{B7}$$

$$\langle\sigma v\rangle_{\phi}^{\text{eff}} = \left[\sum\nolimits_i g_i m_i^2 K_2\left(\frac{m_i}{T}\right)\right]^{-2}\sum_{i,j} 2\langle\sigma v\rangle_{ij\to\phi\phi} g_i g_j m_i^2 m_j^2 K_2\left(\frac{m_i}{T}\right) K_2\left(\frac{m_j}{T}\right), \tag{B8}$$

$$\langle\sigma v\rangle_{\psi_2}^{\text{eff}} = \left[\sum_i g_i m_i^2 K_2\left(\frac{m_i}{T}\right)\right]^{-2}\sum_{i,j} 2\langle\sigma v\rangle_{ij\to\psi_2\bar{\psi}_2} g_i g_j m_i^2 m_j^2 K_2\left(\frac{m_i}{T}\right) K_2\left(\frac{m_j}{T}\right), \tag{B9}$$

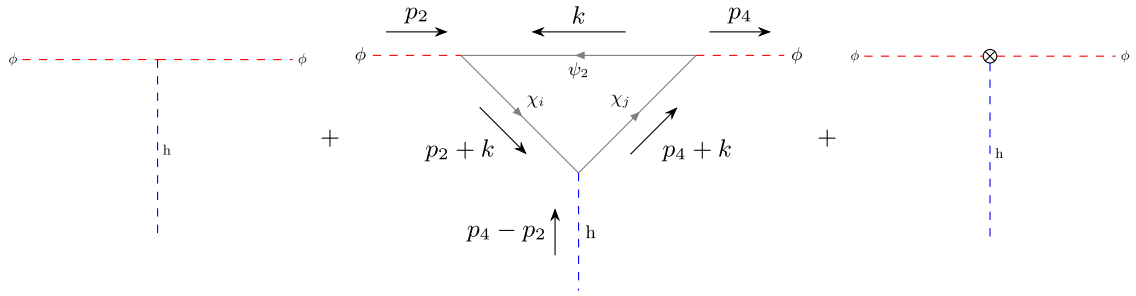

FIG. 18. Tree-level, one-loop, and counterterm interaction vertex for the $h\phi\phi$ interaction vertex where $\{i, j = 1, 2\}$ [89,90].

$$\langle\sigma v\rangle^{\rm eff}_{\rm SM} = \left[\sum_i g_i m_i^2 K_2\left(\frac{m_i}{T}\right)\right]^{-2} \sum_{i,j} 2\langle\sigma v\rangle_{ij\to \rm SM\,SM} g_i g_j m_i^2 m_j^2 K_2\left(\frac{m_i}{T}\right) K_2\left(\frac{m_j}{T}\right). \tag{B10}$$

APPENDIX C: RELEVANT FERMION LOOP CALCULATIONS FOR DIRECT SEARCH

We consider first the three-point vertex and its one-loop contribution for the $\phi\phi h$ interaction, which plays a crucial role in the direct detection of the pFIMP. The one-loop amplitude can be written as a sum of three contributions, the tree-level amplitude, one loop, and counterterm:

$$\mathbb{L}_h = -i\lambda_{h\phi\phi} + \sum_{i,j=1,2} \Gamma^{1-\rm loop}_{ij} + \delta^{\lambda}_{ij}. \tag{C1}$$

Here we have assumed that at tree level $\lambda_{\phi H}$ is very small. The one-loop diagram contributing to $h\phi\phi$ vertex is shown in the middle of Fig. 18, and the amplitude is given by

$$\begin{aligned}\Gamma^{1-\rm loop}_{ij} &= \int \frac{d^4k}{(2\pi)^4}(-1){\rm Tr}\left[\frac{(-i\lambda_{\phi\psi_2\chi_j})i(\not{k} + m_{\psi_2})}{[k^2 - m^2_{\psi_2} + i\epsilon]}\frac{(-i\lambda_{\phi\psi_2\chi_i})i(\not{p}_2 + \not{k} + m_{\chi_i})}{[(p_2+k)^2 - m^2_{\chi_i} + i\epsilon]}\frac{(-i\lambda_{h\chi_i\chi_j})i(\not{p}_4 + \not{k} + m_{\chi_j})}{[(p_4+k)^2 - m^2_{\chi_j} + i\epsilon]}\right],\\
&= -4\int \frac{d^4k}{(2\pi)^4}\frac{m_{\chi_i}m_{\chi_j}m_{\psi_2} + m_{\psi_2}(m^2_\phi - \frac{t}{2}) + (m_{\chi_i} + m_{\chi_j} + m_{\psi_2})k^2 + (m_{\psi_2} + m_{\chi_j})k.p_2 + (m_{\psi_2} + m_{\chi_i})k.p_4}{[k^2 - m^2_{\psi_2} + i\epsilon][(k+p_2)^2 - m^2_{\chi_i} + i\epsilon][(k+p_4)^2 - m^2_{\chi_j} + i\epsilon]}\\
&\quad \times \lambda_{h\chi_i\chi_j}\lambda_{\phi\psi_2\chi_j}\lambda_{\phi\psi_2\chi_i}.\end{aligned} \tag{C2}$$

Using, $l = k + yp_2 + zp_4$,

$$\begin{aligned}\Delta_{ij} &= (y+z)(y+z-1)m^2_\phi - tyz + xm^2_{\psi_2} + ym^2_{\chi_i} + zm^2_{\chi_j},\\
\delta m_{ij} &= m_{\psi_2}\left(m_{\chi_i}m_{\chi_j} + m^2_\phi(1-y-z)^2 - \frac{t}{2}(1-y-z+2yz)\right) + m^2_\phi(m_{\chi_i} + m_{\chi_j})(y+z)(y+z-1)\\
&\quad + \frac{t}{2}m_{\chi_i}y(1-2z) + \frac{t}{2}m_{\chi_j}z(1-2y), \quad \text{and} \quad c_{ij} = m_{\psi_2} + m_{\chi_i} + m_{\chi_j}.\end{aligned}$$

Therefore,

$$\begin{aligned}\Gamma^{1-\rm loop}_{ij} &= -8\lambda_{h\chi_i\chi_j}\lambda_{\phi\psi_2\chi_j}\lambda_{\phi\psi_2\chi_i}\int\frac{d^4l}{(2\pi)^4}\int_0^1 dxdydz\frac{\delta m_{ij} + c_{ij}l^2}{(l^2 - \Delta_{ij} + i\epsilon)^3}\delta(x+y+z-1)\\
&= 8i\lambda_{h\chi_i\chi_j}\lambda_{\phi\psi_2\chi_j}\lambda_{\phi\psi_2\chi_i}\int_0^1 dxdydz\left[\frac{\delta m_{ij}}{32\pi^2}\frac{\Gamma(1+\epsilon)}{\Delta^{1+\epsilon}_{ij}}(4\pi\mu^2)^\epsilon - \frac{c_{ij}}{32\pi^2}(2-\epsilon)\frac{\Gamma(\epsilon)}{\Delta^{\epsilon}_{ij}}(4\pi\mu^2)^\epsilon\right]\delta(x+y+z-1).\end{aligned} \tag{C3}$$

In the above, μ is the dimension regularization parameter (basically a mass scale) introduced to keep λ dimensionless and $d = 4 - 2\epsilon$, in the limit $\epsilon \to 0_+$. At $\epsilon \to 0_+$ limit we have the following expansions:

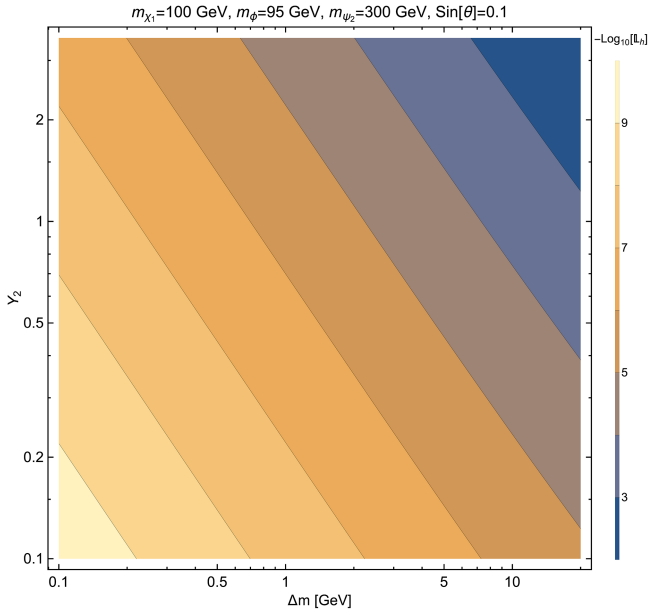

FIG. 19. One-loop amplitude for the Higgs-mediated process.

$$\Gamma(\epsilon) \simeq \frac{1}{\epsilon} - \gamma_E + \mathcal{O}(\epsilon),$$
$$\frac{1}{\Delta^\epsilon} \simeq 1 - \frac{\epsilon}{2}\ln\Delta^2 + \mathcal{O}(\epsilon),$$
$$\mu^\epsilon \simeq 1 + \frac{\epsilon}{2}\ln\mu^2 + \mathcal{O}(\epsilon), \tag{C4}$$

where $\gamma_E \approx 0.5772156649$ is the Euler-Mascheroni constant. Note that we have multiplied Eq. (C3) by a factor of 2 because of the antiparticles in the loop, which also contributes equally. Then,

$$\Gamma^{1-\text{loop}}_{ij} = \frac{i}{2\pi^2}\lambda_{h\chi_i\chi_j}\lambda_{\phi\psi_2\chi_j}\lambda_{\phi\psi_2\chi_i}\int_0^1 dxdydz \times \left[\frac{\delta m_{ij}}{\Delta_{ij}} - 2c_{ij}\left(\frac{1}{\epsilon} - \gamma_E + \ln[4\pi] - \frac{1}{2} + \ln\frac{\mu^2}{\Delta_{ij}}\right) + \mathcal{O}(\epsilon)\right]\delta(x+y+z-1). \tag{C5}$$

Here, we are using the on-shell renormalization scheme to remove the divergence from $\sum_{i,j}\Gamma^{1-\text{loop}}_{ij}$ by calculating the total counterterm $\sum_{i,j}\delta^\lambda_{ij}$ from Higgs mediated annihilation amplitude $\sum_{i,j}\Gamma'^{1-\text{loop}}_{ij} \equiv \sum_{i,j}\Gamma^{1-\text{loop}}_{ij}(p_4 \to -p_4)$, and we are choosing the DM relic density observation scale as the physical renormalization scale, i.e., $q_h^2 = (p_2 + p_4)^2 = 4m_\phi^2$ [53], to cancel the pole in the Eq. (C5),

$$\sum_{i,j}\delta^\lambda_{ij} = -\sum_{i,j}\Gamma'^{1-\text{loop}}_{ij}\Big|_{q_h^2\to 4m_\phi^2}. \tag{C6}$$

The total amplitude at $\epsilon \to 0$ and $t \to 0$ then becomes

$$\mathbb{L}_h = -i\lambda_{h\phi\phi} + \sum_{i,j}\Gamma^{1-\text{loop}}_{ij}\Big|_{t\to 0} - \sum_{i,j}\Gamma'^{1-\text{loop}}_{ij}\Big|_{q_h^2\to 4m_\phi^2}, \tag{C7}$$

with

$$\lambda_{h\bar{\chi}_2\chi_2} = \frac{Y_1}{\sqrt{2}}\sin 2\theta,$$
$$\lambda_{h\bar{\chi}_1\chi_1} = -\frac{Y_1}{\sqrt{2}}\sin 2\theta,$$
$$\lambda_{\phi\psi_2\bar{\chi}_2} = \lambda_{\phi\bar{\psi}_2\chi_2} = Y_2\sin\theta,$$
$$\lambda_{\phi\psi_2\bar{\chi}_1} = \lambda_{\phi\bar{\psi}_2\chi_1} = -Y_2\cos\theta,$$
$$\lambda_{h\bar{\chi}_1\chi_2} = \lambda_{h\bar{\chi}_2\chi_1} = -\frac{Y_1}{\sqrt{2}}\cos 2\theta.$$

In Fig. 19, we show the variation of Higgs-mediated loop amplitude $\mathbb{L}_h$ in the color bar in the Δm-Y_2 plane.

Next, we calculate the one-loop contribution of the Z-mediated diagram, see Fig. 20, for the pFIMP-nucleon direct search cross section:

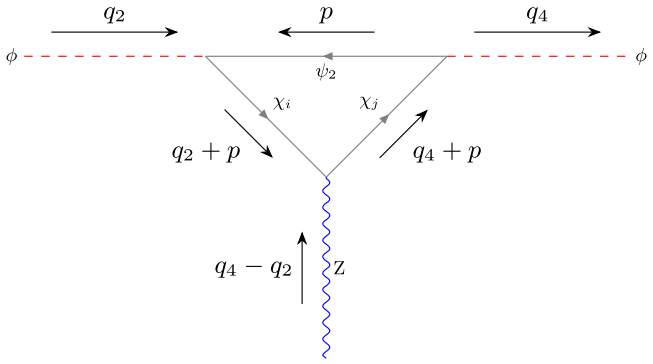

FIG. 20. One-loop Feynman diagrams contributing to the $Z\phi\phi$ interaction term, where $\{i, j = 1, 2\}$.

$$\mathbb{L}^{ij}_\mu = (-1)\int\frac{d^4p}{(2\pi)^4}\text{Tr}\left[\frac{(-i\lambda_{\phi\psi_2\chi_j})i(\not{p}+m_{\psi_2})}{[p^2-m^2_{\psi_2}+i\epsilon]}\frac{(-i\lambda_{\phi\psi_2\chi_i})i(\not{q}_2+\not{p}+m_{\chi_i})}{[(q_2+p)^2-m^2_{\chi_i}+i\epsilon]}\frac{(-i\gamma_\mu\lambda_{Z\chi_i\chi_j})i(\not{q}_4+\not{p}+m_{\chi_j})}{[(q_4+p)^2-m^2_{\chi_j}+i\epsilon]}\right],$$
$$= -4\lambda_{\phi\psi_2\chi_j}\lambda_{\phi\psi_2\chi_i}\lambda_{Z\chi_i\chi_j}\int\frac{d^4p}{(2\pi)^4}\left[\frac{(m_{\psi_2}m_{\chi_j}+p.p+p.q_4)q_{2_\mu}+(m_{\psi_2}m_{\chi_i}+p.p+p.q_2)q_{4_\mu}}{[p^2-m^2_{\psi_2}+i\epsilon][(q_2+p)^2-m^2_{\chi_i}+i\epsilon][(q_4+p)^2-m^2_{\chi_j}+i\epsilon]}\right.$$
$$\left.+\frac{(m_{\chi_i}m_{\chi_j}+m_{\psi_2}m_{\chi_i}+m_{\psi_2}m_{\chi_j}+p.p-q_2.q_4)p_\mu}{[p^2-m^2_{\psi_2}+i\epsilon][(q_2+p)^2-m^2_{\chi_i}+i\epsilon][(q_4+p)^2-m^2_{\chi_j}+i\epsilon]}\right]. \tag{C8}$$

Using Feynman parametrization $l = p + yq_2 + zq_4$, we define,

$$\Delta^{ij} = (y+z)(y+z-1)m_\phi^2 - tyz + xm_{\psi_2}^2 + ym_{\chi_i}^2 + zm_{\chi_j}^2, \tag{C9}$$

$$\begin{aligned}\delta m_\mu^{ij} = {} & [m_{\psi_2}m_{\chi_j} - (m_{\psi_2}m_{\chi_j} + m_{\psi_2}m_{\chi_i} + m_{\chi_i}m_{\chi_j})y + tyz(y-1) - m_\phi^2(z + (y-1)(y+z)^2)]q_{2_\mu} \\ & + [m_{\psi_2}m_{\chi_i} - (m_{\psi_2}m_{\chi_i} + m_{\psi_2}m_{\chi_j} + m_{\chi_i}m_{\chi_j})z + tyz(z-1) - m_\phi^2(y + (z-1)(y+z)^2)]q_{4_\mu},\end{aligned} \tag{C10}$$

$$c_\mu = (1-y)q_{2_\mu} + (1-z)q_{4_\mu}, \tag{C11}$$

and using the dimensional regularization method, we can write,

$$\begin{aligned}\mathbb{L}_\mu^{ij} &= -8\lambda_{\phi\psi_2\chi_j}\lambda_{\phi\psi_2\chi_i}\lambda_{Z\chi_i\chi_j}\int_0^1 dxdydz\int\frac{d^4l}{(2\pi)^4}\frac{\delta m_\mu^{ij} + c_\mu l^2 - 2yq_2^\alpha l_\alpha l_\mu - 2zq_4^\beta l_\beta l_\mu}{[l^2 - \Delta^{ij} + i\epsilon]^3}\delta(x+y+z-1) \\ &= \frac{i}{4\pi^2}\lambda_{\phi\psi_2\chi_j}\lambda_{\phi\psi_2\chi_i}\lambda_{Z\chi_i\chi_j}\int_0^1 dxdydz\left[\frac{\delta m_\mu^{ij}}{\Delta^{ij}} - (2c_\mu - yq_{2_\mu} - zq_{4_\mu})\left(\frac{1}{\epsilon} - \gamma_E + \ln[4\pi\mu^2] - \ln\Delta^{ij}\right)\right. \\ &\quad \left. + c_\mu + \mathcal{O}(\epsilon)\right]\delta(x+y+z-1),\end{aligned} \tag{C12}$$

where

$$\begin{aligned}\lambda_{\phi\psi_2\bar{\chi}_1} &= \lambda_{\phi\bar{\psi}_2\chi_1} = -Y_2\cos\theta, \\ \lambda_{\phi\psi_2\bar{\chi}_2} &= \lambda_{\phi\bar{\psi}_2\chi_2} = Y_2\sin\theta, \\ \lambda_{Z\bar{\chi}_1\chi_1} &= \frac{g}{2\cos\theta_w}\sin^2\theta = \frac{m_Z}{v}\sin^2\theta, \\ \lambda_{Z\bar{\chi}_2\chi_2} &= \frac{g}{2\cos\theta_w}\cos^2\theta = \frac{m_Z}{v}\cos^2\theta, \\ \lambda_{Z\bar{\chi}_1\chi_2} &= \lambda_{Z\bar{\chi}_2\chi_1} = \frac{g}{2\cos\theta_w}\sin\theta\cos\theta = \frac{m_Z}{v}\sin\theta\cos\theta.\end{aligned}$$

In a similar way to the Higgs mediated diagram, a factor of 2 has been multiplied in Eq. (C12) for the antiparticles in the loop, and the total amplitude becomes

$$\begin{aligned}\mathbb{L}_\mu^Z &= 2\sum_{i,j=1,2}\mathbb{L}_\mu^{ij}, \\ &= \frac{i}{2\pi^2}\sum_{i,j=1,2}\lambda_{\phi\psi_2\chi_j}\lambda_{\phi\psi_2\chi_i}\lambda_{Z\chi_i\chi_j}\int_0^1 dxdydz\left[\frac{\delta m_\mu^{ij}}{\Delta^{ij}}\right. \\ &\quad \left. - (2c_\mu - yq_{2_\mu} - zq_{4_\mu})\left(\frac{1}{\epsilon} - \gamma_E + \ln[4\pi\mu^2] - \ln\Delta^{ij}\right) + c_\mu + \mathcal{O}(\epsilon)\right]\delta(x+y+z-1), \\ &\underset{\epsilon\to 0}{=} \frac{i}{2\pi^2}\sum_{i,j=1,2}\lambda_{\phi\psi_2\chi_j}\lambda_{\phi\psi_2\chi_i}\lambda_{Z\chi_i\chi_j}\int_0^1 dxdydz\left[\frac{\delta m_\mu^{ij}}{\Delta^{ij}} + (2c_\mu - yq_{2_\mu} - zq_{4_\mu})\ln\Delta^{ij}\right]\delta(x+y+z-1), \\ &\xrightarrow[m_{\chi_1}=m_{\chi_2}]{} 0, \\ &\xrightarrow[m_{\chi_1}\neq m_{\chi_2}]{} \mathbb{L}_Z(q_{2_\mu} + q_{4_\mu}).\end{aligned}$$

We have cross-checked our analytical solution with Package-X [91] and FeynCalc [92]. In Fig. 21, the color bar represents the variation of Z-mediated loop amplitude $\mathbb{L}_Z$ in Δm-Y_2 plane.

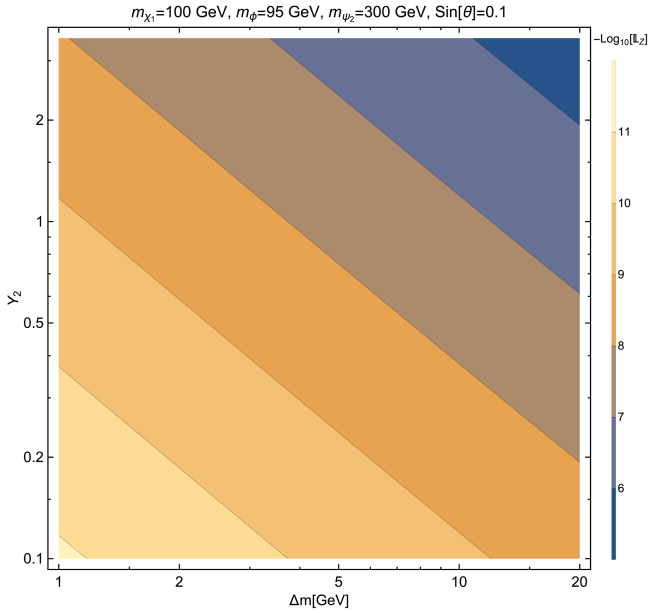

FIG. 21. One-loop amplitude for the Z-mediated process.

APPENDIX D: DIRECT DETECTION CROSS SECTION OF PFIMP AND WIMP

After the amplitude, we calculate the cross section here. The Feynman diagrams for DM ϕ scattering off a nucleon at tree-level and one-loop level are shown in Fig. 10. For the Higgs mediator, the tree-level contribution is negligible because of tiny $h\phi\phi$ coupling that we have assumed, justifiably, in the pFIMP scenario. The dominant Higgs-mediated contribution therefore comes from the one-loop diagram. The two interaction vertices involved in the loop-induced Higgs-mediated process are $\mathbb{L}_h h\phi\phi$ and $\frac{m_q}{v} hq\bar{q}$; the effective Lagrangian at the parton level can be written as

$$\mathcal{L}^h_{\text{eff}} = \mathbb{L}_h \frac{m_q}{v}\frac{1}{m_h^2} q\bar{q}\phi\phi = f^h_q q\bar{q}\phi\phi. \tag{D1}$$

The matrix element for a scattering $N\phi \to N\phi$ via Higgs mediation, where N stands for nucleon, is the following:

$$i\mathcal{M}^h_{N\phi} = \alpha^h_N[\bar{u}_N(q_3)u_N(q_1)], \tag{D2}$$

where α^h_N is the effective DM-nucleon coupling and the relation with quark level coupling is

$$\frac{\alpha^h_N}{m_N} = \sum_{q=u,d,s} f^N_{T_q}\frac{f^{\text{h}}_q}{m_q} + \frac{2}{27}\left(1 - \sum_{q=u,d,s} f^N_{T_q}\right)\sum_{q=c,b,t}\frac{f^{\text{h}}_q}{m_q}. \tag{D3}$$

The nuclear form factors are defined by [93,94]

$$\langle N|m_q\bar{q}q|N\rangle \equiv m_N f^N_{T_q}\langle N|N\rangle (q = u, d, s). \tag{D4}$$

See Table IV for the numerical values of the form factors. The matrix element squared for the Higgs mediated process then turns out to be

$$\overline{|\mathcal{M}^h_{N\phi}|^2} = \frac{1}{2}\sum_{\text{all spin}} |\mathcal{M}^h_{N\phi}|^2 = 4m_N^2|\alpha^h_N|^2. \tag{D5}$$

The effective Lagrangian for Z-mediator direct search process can be written as

$$\begin{aligned}\mathcal{L}^Z_{\text{eff}} &= \bar{q}\left[\frac{g}{\cos\theta_W}\gamma^\mu\frac{1}{2}(c^q_V - c^q_A\gamma^5)\right] q\frac{\mathbb{L}_Z}{m_Z^2}\phi(q_{2_\mu} + q_{4_\nu})\phi, \quad \text{(SI + SD)}\\ &\to \frac{m_Z}{v}c^q_V\frac{\mathbb{L}_Z}{m_Z^2}\bar{q}\gamma^\mu q\phi(q_{2_\mu} + q_{4_\mu})\phi, \quad \text{(SI)}\\ &= \frac{c^q_V}{v}\frac{\mathbb{L}_Z}{m_Z}\bar{q}\gamma^\mu q\phi(q_{2_\mu} + q_{4_\mu})\phi,\\ &= b^Z_q\bar{q}\gamma^\mu q\phi(q_{2_\mu} + q_{4_\mu})\phi.\end{aligned} \tag{D6}$$

The matrix element for Z-mediated pFIMP-nucleon scattering $N\phi \to N\phi$ is as follows, assuming Let, $\mathbb{L}^Z_\mu = \mathbb{L}_Z(q_{2_\mu} + q_{4_\mu})$,

$$i\mathcal{M}^Z_{N\phi} = b^Z_N[\bar{u}_N(q_3)\gamma^\mu u_N(q_1)](q_{2_\mu} + q_{4_\mu}). \tag{D7}$$

Here b^Z_N is the DM–nucleon effective coupling. As the sea quarks and the gluons do not contribute to the vector current, only valence quark contributions add up due to the conservation of the vector current, which gives us $b_p = 2b_u + b_d$ and $b_n = b_u + 2b_d$. So the effective DM-nucleon couplings can be recast in terms of quark level couplings as [95]

$$\begin{aligned} b^Z_p &= 2b^Z_u + b^Z_d,\\ b^Z_n &= b^Z_u + 2b^Z_d; \quad \text{where } b^Z_q = \frac{c^q_V}{v}\frac{\mathbb{L}_Z}{m_Z}.\end{aligned} \tag{D8}$$

The matrix element squared turns out to be

TABLE IV. Values of the nuclear form factors $f^N_{T_{q,G}}$.

Nucleon	$f^N_{T_u}$	$f^N_{T_d}$	$f^N_{T_s}$	$f^N_{T_G}$	$f^N_{T_c}$	$f^N_{T_b}$	$f^N_{T_t}$
Proton	0.018(5)	0.027(7)	0.037(17)	0.917(19)	0.078(2)	0.072(2)	0.069(1)
Neutron	0.013(3)	0.040(10)	0.037(17)	0.910(20)	0.078(2)	0.071(2)	0.068(2)

$$\begin{aligned}\overline{|\mathcal{M}^Z_{N\phi}|^2} &= \frac{|b^Z_N|^2}{2}\mathrm{Tr}[(\not{q}_3 + m_N)\gamma^\mu(\not{q}_1 + m_N)\gamma^\nu](q_{2_\mu} + q_{4_\mu})(q_{2_\nu} + q_{4_\nu}),\\ &= 4|b^Z_N|^2 4m_\phi^2 m_N^2 \quad \text{as initially the nucleus is in rest, } q_1 \sim \{m_N, \vec{0}\}. \end{aligned} \tag{D9}$$

The Z and Higgs mediated cross term is

$$\begin{aligned}\overline{|\mathcal{M}^Z_{N\phi}|^\dagger|\mathcal{M}^h_{N\phi}|} &= \frac{1}{2}\sum_{\text{all spin}}[b^Z_N(\bar{u}_N(q_3)\gamma^\mu u_N(q_1))(q_{2_\mu} + q_{4_\mu})]^\dagger[\alpha^h_N(\bar{u}_N(q_3)u_N(q_1))],\\ &= 2m_N b^{Z^\dagger}_N \alpha^h_N 4m_\phi m_N, \quad \text{as initially the nucleus is in rest, } q_1 \sim \{m_N, \vec{0}\}\\ &= 8m_N^2 m_\phi b^{Z^\dagger}_N \alpha^h_N. \end{aligned} \tag{D10}$$

In a similar way,

$$\begin{aligned}\overline{|\mathcal{M}^Z_{N\phi}||\mathcal{M}^h_{N\phi}|^\dagger} &= \frac{1}{2}\sum_{\text{all spin}}[b^Z_N(\bar{u}_N(q_3)\gamma^\mu u_N(q_1))(q_{2_\mu} + q_{4_\mu})][\alpha^h_N(\bar{u}_N(q_3)u_N(q_1))]^\dagger,\\ &= 8m_N^2 m_\phi b^Z_N \alpha^{h^\dagger}_N. \end{aligned} \tag{D11}$$

The spin-independent pFIMP – nucleon scattering cross section in the nonrelativistic limit, assuming the initial nucleon is at rest, is given by [96]

$$\begin{aligned}\sigma_{\phi N} &= \frac{1}{4m_\phi m_N|w - v_N|}\int \frac{d^3q_3}{(2\pi)^3 2m_N}\frac{d^3q_4}{(2\pi)^3 2m_\phi}\overline{|\mathcal{M}^Z_{N\phi} + \mathcal{M}^h_{N\phi}|^2}(2\pi)^4\delta^4(q_1 + q_2 - q_3 - q_4)\\ &= \int \frac{\overline{|\mathcal{M}^Z_{N\phi} + \mathcal{M}^h_{N\phi}|^2}}{4\pi^2(4m_\phi m_N)^2|w - v_N|}d^3q_3 d^3q_4\delta(E_1 + E_2 - E_3 - E_4)\delta^3(\vec{q}_1 + \vec{q}_2 - \vec{q}_3 - \vec{q}_4). \end{aligned} \tag{D12}$$

From energy conservation,

$$\begin{aligned}2\mu_{\phi N}\vec{q}_2.\vec{q}_3 &= m_\phi|\vec{q}_3|^2,\\ |\vec{q}_3| &= 2\mu_{\phi N} w\cos\theta, \end{aligned} \tag{D13}$$

where w, v_N are the initial velocities of DM and the nucleus. We have assumed that in Lab-frame, the nucleus initially is at rest, $|\vec{v}_N| = 0$, so the relative velocity between DM and nucleus becomes w. The angle between $\vec{q}_2$ and $\vec{q}_3$ is θ. Then Eq. (D12) becomes

$$\begin{aligned}\sigma_{\phi N} &= \int \frac{\overline{|\mathcal{M}^Z_{N\phi} + \mathcal{M}^h_{N\phi}|^2}}{4\pi^2(4m_\phi m_N)^2 w}(\pi|\vec{q}_3|d\cos\theta d|\vec{q}_3|^2)d^3q_4\delta(E_1 + E_2 - E_3 - E_4)\delta^3(\vec{q}_2 - \vec{q}_3 - \vec{q}_4),\\ &= \frac{\mu^2_{\phi N}}{4\pi m^2_\phi}\left|\alpha^h_N + 2m_\phi b^{Z^\dagger}_N\right|^2. \end{aligned} \tag{D14}$$

Let us now turn to WIMP direct search cross section. The Feynman diagrams corresponding to WIMP DM χ_1 scattering off a nucleon at tree level are shown in Fig. 8. The two relevant interaction vertices for Higgs mediated interaction are $\lambda_{h\chi_1\bar{\chi}_1}h\chi_1\bar{\chi}_1$ and $\frac{m_q}{v}hq\bar{q}$. The effective Lagrangian for spin-independent direct search process can be written as

$$\mathcal{L}^h_{\text{eff}} = \frac{m_q}{v}\frac{1}{m_h^2}\lambda_{h\chi_1\bar{\chi}_1} q\bar{q}\chi_1\bar{\chi}_1 = F^h_q q\bar{q}\chi_1\bar{\chi}_1, \tag{D15}$$

where $\lambda_{h\chi_1\bar{\chi}_1} = -\frac{Y_1}{\sqrt{2}}\sin 2\theta$ in our model. The matrix element for a scattering $N\chi_1 \to N\chi_1$ via Higgs mediation (N stands for nucleon) is the following:

$$i\mathcal{M}^h_{N\chi_1} = \beta^h_N[\bar{u}_N(q_3)u_N(q_1)][\bar{u}_{\chi_1}(q_4)u_{\chi_1}(q_2)], \tag{D16}$$

where β^h_N is the DM-nucleon coupling, related to the quark level coupling F^h_q following Eq. (D3). The amplitude squared is

$$\overline{|\mathcal{M}^h_{N\chi_1}|^2} = \frac{1}{4}\sum_{\text{spin}}|\mathcal{M}^h_{N\chi_1}|^2 = 16m^2_{\chi_1}m^2_N|\beta^h_N|^2. \tag{D17}$$

For Z mediator, only the vector term contributes to the spin-independent (SI) cross section, and the effective Lagrangian is

$$\begin{aligned}\mathcal{L}^Z_{\text{eff}} &= \frac{m_Z}{v}\frac{1}{m_Z^2}\lambda_{Z\chi_1\bar{\chi}_1}\bar{q}\gamma^\mu(c^q_V - c^q_A\gamma^5)q\bar{\chi}_1\gamma_\mu\chi_1 \quad \text{(SI + SD)}\\ &\to \frac{m_Z}{v}\frac{c^q_V}{m_Z^2}\lambda_{Z\chi_1\bar{\chi}_1}\bar{q}\gamma^\mu q\bar{\chi}_1\gamma_\mu\chi_1 \quad \text{(SI)}\\ &= B_q\bar{\chi}_1\gamma^\mu\chi_1\bar{q}\gamma_\mu q,\end{aligned} \tag{D18}$$

where, $\lambda_{Z\chi_1\bar{\chi}_1} = \frac{m_Z}{v}\sin^2\theta$.

The matrix element for $N\chi_1 \to N\chi_1$ scattering via Z mediation is

$$i\mathcal{M}^Z_{N\chi_1} = B^Z_N[\bar{u}_N(q_3)\gamma^\mu u_N(q_1)][\bar{u}_{\chi_1}(q_4)\gamma_\mu u_{\chi_1}(q_2)], \tag{D19}$$

where B^Z_N is the DM-nucleon coupling and is related to the quark level coupling B_q followed by the Eq. (D8). Finally, the amplitude squared for Z mediation is

$$\overline{|\mathcal{M}^Z_{N\chi_1}|^2} = \frac{1}{4}\sum_{\text{spin}}|\mathcal{M}^Z_{N\chi_1}|^2 = 16m^2_{\chi_1}m^2_N|B^Z_N|^2. \tag{D20}$$

In a two-component framework, the effective spin-independent $\chi_1 N$ scattering cross section becomes [3,97]

$$\sigma^{\text{SI}}_{\chi_1 N_{\text{eff}}} = \frac{\Omega_{\chi_1}}{\Omega_{\chi_1}+\Omega_\phi}\frac{\mu^2_{\chi_1 N}}{\pi}|\beta^h_N + B^Z_N|^2, \tag{D21}$$

where $\mu_{\chi_1 N} = m_{\chi_1}m_N/(m_{\chi_1}+m_N)$ is the WIMP-nucleon reduced mass, with $m_N \sim 0.939$ GeV. The Z mediated direct search for the WIMP provides a stringent constraint on the WIMP parameter space reducing the singlet-doublet mixing angle significantly.

[1] N. Aghanim *et al.* (Planck Collaboration), Planck 2018 results. VI. Cosmological parameters, Astron. Astrophys. **641**, A6 (2020); **652**, C4(E) (2021).

[2] P. Gondolo and G. Gelmini, Cosmic abundances of stable particles: Improved analysis, Nucl. Phys. **B360**, 145 (1991).

[3] G. Jungman, M. Kamionkowski, and K. Griest, Supersymmetric dark matter, Phys. Rep. **267**, 195 (1996).

[4] Y. Hochberg, E. Kuflik, T. Volansky, and J. G. Wacker, Mechanism for thermal relic dark matter of strongly interacting massive particles, Phys. Rev. Lett. **113**, 171301 (2014).

[5] L. J. Hall, K. Jedamzik, J. March-Russell, and S. M. West, Freeze-in production of FIMP dark matter, J. High Energy Phys. 03 (2010) 080.

[6] J. McDonald, Thermally generated gauge singlet scalars as self-interacting dark matter, Phys. Rev. Lett. **88**, 091304 (2002).

[7] M. Kaplinghat, S. Tulin, and H.-B. Yu, Direct detection portals for self-interacting dark matter, Phys. Rev. D **89**, 035009 (2014).

[8] D. Pappadopulo, J. T. Ruderman, and G. Trevisan, Dark matter freeze-out in a nonrelativistic sector, Phys. Rev. D **94**, 035005 (2016).

[9] E. Aprile *et al.* (XENON Collaboration), Dark matter search results from a one ton-year exposure of XENON1T, Phys. Rev. Lett. **121**, 111302 (2018).

[10] E. Aprile *et al.* (XENON Collaboration), Projected WIMP sensitivity of the XENONnT dark matter experiment, J. Cosmol. Astropart. Phys. 11 (2020) 031.

[11] E. Aprile *et al.* (XENON Collaboration), Search for new physics in electronic recoil data from XENONnT, Phys. Rev. Lett. **129**, 161805 (2022).

[12] E. Aprile *et al.* (XENON Collaboration), First dark matter search with nuclear recoils from the XENONnT experiment, Phys. Rev. Lett. **131**, 041003 (2023).

[13] C. Cheng *et al.* (PandaX-II Collaboration), Search for light dark matter-electron scatterings in the PandaX-II experiment, Phys. Rev. Lett. **126**, 211803 (2021).

[14] Y. Meng *et al.* (PandaX-4T Collaboration), Dark matter search results from the PandaX-4T commissioning run, Phys. Rev. Lett. **127**, 261802 (2021).

[15] J. Aalbers *et al.* (LZ Collaboration), First dark matter search results from the LUX-ZEPLIN (LZ) experiment, Phys. Rev. Lett. **131**, 041002 (2023).
[16] J. Goodman, M. Ibe, A. Rajaraman, W. Shepherd, T. M. P. Tait, and H.-B. Yu, Constraints on light Majorana dark matter from colliders, Phys. Lett. B **695**, 185 (2011).
[17] J. Goodman, M. Ibe, A. Rajaraman, W. Shepherd, T. M. P. Tait, and H.-B. Yu, Constraints on dark matter from colliders, Phys. Rev. D **82**, 116010 (2010).
[18] A. Rajaraman, W. Shepherd, T. M. P. Tait, and A. M. Wijangco, LHC bounds on interactions of dark matter, Phys. Rev. D **84**, 095013 (2011).
[19] P. J. Fox, R. Harnik, J. Kopp, and Y. Tsai, Missing energy signatures of dark matter at the LHC, Phys. Rev. D **85**, 056011 (2012).
[20] O. Buchmueller, M. J. Dolan, and C. McCabe, Beyond effective field theory for dark matter searches at the LHC, J. High Energy Phys. 01 (2014) 025.
[21] A. A. Petrov and W. Shepherd, Searching for dark matter at LHC with Mono-Higgs production, Phys. Lett. B **730**, 178 (2014).
[22] W. Altmannshofer, P. J. Fox, R. Harnik, G. D. Kribs, and N. Raj, Dark matter signals in dilepton production at hadron colliders, Phys. Rev. D **91**, 115006 (2015).
[23] R. M. Capdevilla, A. Delgado, A. Martin, and N. Raj, Characterizing dark matter at the LHC in Drell-Yan events, Phys. Rev. D **97**, 035016 (2018).
[24] N. F. Bell, Y. Cai, J. B. Dent, R. K. Leane, and T. J. Weiler, Dark matter at the LHC: Effective field theories and gauge invariance, Phys. Rev. D **92**, 053008 (2015).
[25] Z.-H. Yu, Q.-S. Yan, and P.-F. Yin, Detecting interactions between dark matter and photons at high energy e^+e^- colliders, Phys. Rev. D **88**, 075015 (2013).
[26] R. Essig, J. Mardon, M. Papucci, T. Volansky, and Y.-M. Zhong, Constraining light dark matter with low-energy e^+e^- colliders, J. High Energy Phys. 11 (2014) 167.
[27] K. Kadota and J. Silk, Constraints on light magnetic dipole dark matter from the ILC and SN 1987A, Phys. Rev. D **89**, 103528 (2014).
[28] Z.-H. Yu, X.-J. Bi, Q.-S. Yan, and P.-F. Yin, Dark matter searches in the mono-Z channel at high energy e^+e^- colliders, Phys. Rev. D **90**, 055010 (2014).
[29] A. Freitas and S. Westhoff, Leptophilic dark matter in lepton interactions at LEP and ILC, J. High Energy Phys. 10 (2014) 116.
[30] S. Dutta, D. Sachdeva, and B. Rawat, Signals of leptophilic dark matter at the ILC, Eur. Phys. J. C **77**, 639 (2017).
[31] M. Habermehl, M. Berggren, and J. List, WIMP dark matter at the international linear collider, Phys. Rev. D **101**, 075053 (2020).
[32] E. A. Baltz, M. Battaglia, M. E. Peskin, and T. Wizansky, Determination of dark matter properties at high-energy colliders, Phys. Rev. D **74**, 103521 (2006).
[33] G. Bélanger *et al.*, LHC-friendly minimal freeze-in models, J. High Energy Phys. 02 (2019) 186.
[34] C. Boehm, D. Hooper, J. Silk, M. Casse, and J. Paul, MeV dark matter: Has it been detected?, Phys. Rev. Lett. **92**, 101301 (2004).
[35] C. Boehm, T. A. Ensslin, and J. Silk, Can annihilating dark matter be lighter than a few GeVs?, J. Phys. G **30**, 279 (2004).
[36] S. Stephens, Antiprotons in cosmic rays and their implications, Adv. Space Res. **9**, 55 (1989).
[37] C. S. Shen and G. B. Berkey, Antiprotons and positrons in cosmic rays, Phys. Rev. **171**, 1344 (1968).
[38] F. W. Stecker and A. J. Tylka, The cosmic ray anti-proton spectrum from dark matter annihilation and its astrophysical implications: A new look, Astrophys. J. Lett. **336**, L51 (1989).
[39] C. Evoli, I. Cholis, D. Grasso, L. Maccione, and P. Ullio, Antiprotons from dark matter annihilation in the Galaxy: Astrophysical uncertainties, Phys. Rev. D **85**, 123511 (2012).
[40] T. Delahaye, R. Lineros, F. Donato, N. Fornengo, and P. Salati, Positrons from dark matter annihilation in the galactic halo: Theoretical uncertainties, Phys. Rev. D **77**, 063527 (2008).
[41] L. Bergstrom, T. Bringmann, I. Cholis, D. Hooper, and C. Weniger, New limits on dark matter annihilation from AMS cosmic ray positron data, Phys. Rev. Lett. **111**, 171101 (2013).
[42] A. J. Tylka, Cosmic ray positrons from annihilation of weakly interacting massive particles in the Galaxy, Phys. Rev. Lett. **63**, 840 (1989); **63**, 1658(E) (1989).
[43] Q.-H. Cao, E. Ma, J. Wudka, and C. P. Yuan, Multipartite dark matter, arXiv:0711.3881.
[44] K. M. Zurek, Multi-component dark matter, Phys. Rev. D **79**, 115002 (2009).
[45] S. Profumo, K. Sigurdson, and L. Ubaldi, Can we discover multi-component WIMP dark matter?, J. Cosmol. Astropart. Phys. 12 (2009) 016.
[46] S. Bhattacharya, A. Drozd, B. Grzadkowski, and J. Wudka, Two-component dark matter, J. High Energy Phys. 10 (2013) 158.
[47] B. Díaz Sáez, K. Möhling, and D. Stöckinger, Two real scalar WIMP model in the assisted freeze-out scenario, J. Cosmol. Astropart. Phys. 10 (2021) 027.
[48] G. Belanger and J.-C. Park, Assisted freeze-out, J. Cosmol. Astropart. Phys. 03 (2012) 038.
[49] T. N. Maity and T. S. Ray, Exchange driven freeze out of dark matter, Phys. Rev. D **101**, 103013 (2020).
[50] S. Bhattacharya, P. Ghosh, J. Lahiri, and B. Mukhopadhyaya, Mono-X signal and two component dark matter: New distinction criteria, Phys. Rev. D **108**, L111703 (2023).
[51] S. Bhattacharya, P. Ghosh, J. Lahiri, and B. Mukhopadhyaya, Distinguishing two dark matter component particles at e^+e^- colliders, J. High Energy Phys. 12 (2022) 049.
[52] P. Ghosh, P. Konar, A. K. Saha, and S. Show, Self-interacting freeze-in dark matter in a singlet doublet scenario, J. Cosmol. Astropart. Phys. 10 (2022) 017.
[53] S. Bhattacharya, J. Lahiri, and D. Pradhan, Dynamics of the pseudo-FIMP in presence of a thermal dark matter, Phys. Rev. D **108**, L111702 (2023).
[54] F. del Aguila, L. Ametller, G. L. Kane, and J. Vidal, Vector like fermion and standard Higgs production at hadron colliders, Nucl. Phys. **B334**, 1 (1990).

[55] S. Bhattacharya, P. Ghosh, and N. Sahu, Multipartite dark matter with scalars, fermions and signatures at LHC, J. High Energy Phys. 02 (2019) 059.

[56] A. M. Sirunyan *et al.* (CMS Collaboration), Search for invisible decays of a Higgs boson produced through vector boson fusion in proton-proton collisions at $\sqrt{s} = 13$ TeV, Phys. Lett. B **793**, 520 (2019).

[57] L3 Collaboration, Search for heavy neutral and charged leptons in e^+e^- annihilation at LEP, Phys. Lett. B **517**, 75 (2001).

[58] L3 Collaboration, Search for scalar leptons and scalar quarks at LEP, Phys. Lett. B **580**, 37 (2004).

[59] DELPHI Collaboration, Searches for supersymmetric particles in e^+e^- collisions up to 208-GeV and interpretation of the results within the MSSM, Eur. Phys. J. C **31**, 421 (2003).

[60] OPAL Collaboration, Search for anomalous production of dilepton events with missing transverse momentum in e^+e^- collisions at $\sqrt{s} = 183$-Gev to 209-GeV, Eur. Phys. J. C **32**, 453 (2004).

[61] ALEPH Collaboration, Absolute lower limits on the masses of selectrons and sneutrinos in the MSSM, Phys. Lett. B **544**, 73 (2002).

[62] K. Griest and D. Seckel, Three exceptions in the calculation of relic abundances, Phys. Rev. D **43**, 3191 (1991).

[63] R. T. D'Agnolo, D. Pappadopulo, and J. T. Ruderman, Fourth exception in the calculation of relic abundances, Phys. Rev. Lett. **119**, 061102 (2017).

[64] G. Bélanger, F. Boudjema, A. Pukhov, and A. Semenov, micrOMEGAs4.1: Two dark matter candidates, Comput. Phys. Commun. **192**, 322 (2015).

[65] R. T. D'Agnolo, C. Mondino, J. T. Ruderman, and P.-J. Wang, Exponentially light dark matter from coannihilation, J. High Energy Phys. 08 (2018) 079.

[66] C.-K. Chua and R.-C. Hsieh, Study of Dirac fermionic dark matter, Phys. Rev. D **88**, 036011 (2013).

[67] J. Edsjo and P. Gondolo, Neutralino relic density including coannihilations, Phys. Rev. D **56**, 1879 (1997).

[68] M. Dutta, S. Bhattacharya, P. Ghosh, and N. Sahu, Singlet-doublet majorana dark matter and neutrino mass in a minimal type-I seesaw scenario, J. Cosmol. Astropart. Phys. 03 (2021) 008.

[69] G. Duda, G. Gelmini, P. Gondolo, J. Edsjo, and J. Silk, Indirect detection of a subdominant density component of cold dark matter, Phys. Rev. D **67**, 023505 (2003).

[70] P. Ullio, L. Bergstrom, J. Edsjo, and C. G. Lacey, Cosmological dark matter annihilations into gamma-rays—a closer look, Phys. Rev. D **66**, 123502 (2002).

[71] V. Gammaldi, J. Pérez-Romero, J. Coronado-Blázquez, M. Di Mauro, E. V. Karukes, M. A. Sánchez-Conde, and P. Salucci, Dark matter search in dwarf irregular galaxies with the Fermi Large Area Telescope, Phys. Rev. D **104**, 083026 (2021).

[72] K. Abe *et al.* (Super-Kamiokande Collaboration), Indirect search for dark matter from the Galactic Center and halo with the Super-Kamiokande detector, Phys. Rev. D **102**, 072002 (2020).

[73] H. Abdalla *et al.* (H.E.S.S. Collaboration), Search for dark matter annihilation signals in the H.E.S.S. inner galaxy survey, Phys. Rev. Lett. **129**, 111101 (2022).

[74] M. G. Aartsen *et al.* (IceCube Collaboration), Observation and characterization of a cosmic muon neutrino flux from the northern hemisphere using six years of IceCube data, Astrophys. J. **833**, 3 (2016).

[75] R. Abbasi *et al.* (IceCube Collaboration), Searches for connections between dark matter and high-energy neutrinos with IceCube, J. Cosmol. Astropart. Phys. 10 (2023) 003.

[76] R. Abbasi *et al.* (IceCube Collaboration), Search for GeV-scale dark matter annihilation in the Sun with IceCube DeepCore, Phys. Rev. D **105**, 062004 (2022).

[77] B. Díaz Sáez, P. Escalona, S. Norero, and A. R. Zerwekh, Fermion singlet dark matter in a pseudoscalar dark matter portal, J. High Energy Phys. 10 (2021) 233.

[78] A. Reinert and M. W. Winkler, A precision search for WIMPs with charged cosmic rays, J. Cosmol. Astropart. Phys. 01 (2018) 055.

[79] M. Ackermann *et al.* (Fermi-LAT Collaboration), Searching for dark matter annihilation from Milky Way dwarf spheroidal galaxies with six years of Fermi Large Area Telescope data, Phys. Rev. Lett. **115**, 231301 (2015).

[80] S. Bhattacharya, S. Jahedi, and J. Wudka, Probing heavy charged fermions at e^+e^- collider using the optimal observable technique, J. High Energy Phys. 05 (2022) 009.

[81] G. Guedes and J. Santiago, New leptons with exotic decays: Collider limits and dark matter complementarity, J. High Energy Phys. 01 (2022) 111.

[82] ATLAS Collaboration, A statistical combination of ATLAS Run 2 searches for charginos and neutralinos at the LHC, arXiv:2402.08347.

[83] ATLAS Collaboration, The quest to discover supersymmetry at the ATLAS experiment, arXiv:2403.02455.

[84] CMS Collaboration, Combined search for electroweak production of winos, binos, higgsinos, and sleptons in proton-proton collisions at $\sqrt{s} = 13$ TeV, arXiv:2402.01888.

[85] G. Aad *et al.* (ATLAS Collaboration), Search for invisible Higgs-boson decays in events with vector-boson fusion signatures using 139 fb^{-1} of proton-proton data recorded by the ATLAS experiment, J. High Energy Phys. 08 (2022) 104.

[86] A. Tumasyan *et al.* (CMS Collaboration), Search for invisible decays of the Higgs boson produced via vector boson fusion in proton-proton collisions at $s = 13$ TeV, Phys. Rev. D **105**, 092007 (2022).

[87] R. L. Workman *et al.* (Particle Data Group), Review of particle physics, Prog. Theor. Exp. Phys. **2022**, 083C01 (2022).

[88] CMS Collaboration, Precision measurement of the Z boson invisible width in pp collisions at $\sqrt{s} = 13$ TeV, Phys. Lett. B **842**, 137563 (2023).

[89] M. D. Schwartz, *Quantum Field Theory and the Standard Model* (Cambridge University Press, Cambridge, England, 2014).

[90] M. E. Peskin and D. V. Schroeder, *An Introduction to Quantum Field Theory* (Addison-Wesley, Reading, USA, 1995).

[91] H. H. Patel, Package-X 2.0: A *Mathematica* package for the analytic calculation of one-loop integrals, Comput. Phys. Commun. **218**, 66 (2017).

[92] V. Shtabovenko, R. Mertig, and F. Orellana, FeynCalc 9.3: New features and improvements, Comput. Phys. Commun. **256**, 107478 (2020).

[93] G. Bertone, D. Hooper, and J. Silk, Particle dark matter: Evidence, candidates and constraints, Phys. Rep. **405**, 279 (2005).

[94] J. Ellis, N. Nagata, and K. A. Olive, Uncertainties in WIMP dark matter scattering revisited, Eur. Phys. J. C **78**, 569 (2018).

[95] P. Agrawal, Z. Chacko, C. Kilic, and R. K. Mishra, A classification of dark matter candidates with primarily spin-dependent interactions with matter, arXiv:1003.1912.

[96] T. Lin, Dark matter models and direct detection, Proc. Sci. 333 (**2019**) 009 [arXiv:1904.07915].

[97] J. Hisano, R. Nagai, and N. Nagata, Effective theories for dark matter nucleon scattering, J. High Energy Phys. 05 (2015) 037.